# Geometrically nonlinear analysis of thin-shell structures based on an isogeometric-meshfree coupling approach

Weidong Li[a], Nhon Nguyen-Thanh[a,*], Kun Zhou[a,*]

[a]*School of Mechanical and Aerospace Engineering, Nanyang Technological University, 50 Nanyang Avenue, Singapore 639798, Singapore*

**Abstract**

This paper develops a novel coupling approach of the isogeometric analysis (IGA) method and the meshfree method for geometrically nonlinear analysis of thin-shell structures. The Kirchhoff-Love (KL) thin-shell theory is employed without the consideration of rotational degrees of freedom. Both parametric domain and physical domain are utilized for the thin-shell structures, and the former one is used to couple the IGA and meshfree methods and to obtain the later one via mapping. The domain is divided into three subdomains: the subdomain described by the IGA method to ensure geometry exactness, the subdomain described by the meshfree method to achieve local refinement, and the coupling subdomain described by both methods. In the coupling subdomain, the reproducing points are obtained based on the consistency conditions to realize smoothness between the IGA and meshfree subdomains. The coupling approach can achieve a higher convergence rate than the IGA and meshfree methods because of the realization of local refinement. The accuracy and robustness of the coupling approach are validated by solving shell benchmark problems.

*Keywords:* Isogeometric Analysis, Meshfree Method, Thin-shell Structure, Consistency Condition

## 1. Introduction

Shell structures play an important role in industrial applications such as turbine disks, water tanks and aircraft. Two different types of shells can be differentiated by the ratio of the thickness $t$ to the radius of curvature $R$ of the middle surface: thin shells ($R/t \geqslant 20$) and thick shells ($R/t < 20$). The deformation of thin shells includes the membrane strains and bending strains without considering the transverse shear strains that are related to the rotational degrees of freedom. The thin-shell analyses are based on the Kirchhoff-Love (KL) theory which requires the continuity of first-order derivatives of displacements ($C^1$ continuity) [1, 2, 3, 4, 5]. The thick-shell analyses are based on the Mindlin-Reissner theory that requires only the continuity of displacements ($C^0$ continuity) [6, 7, 8, 9].

The $C^1$ continuity is difficult to implement with Lagrange polynomial basis functions in the traditional finite element method (FEM) [10, 11]. Various methods have been proposed to formulate $C^1$ conforming thin-shell finite elements. Rectangular shell elements constructed with bicubic

*Corresponding authors. Email addresses: thanhnhon@ntu.edu.sg (Nhon Nguyen-Thanh), kzhou@ntu.edu.sg (Kun Zhou)

Hermite polynomials and triangular shell elements with quintic polynomials have been introduced to interpolate field variables, whereas the computational cost is rather high [12]. Other shell finite elements such as reduced-integration Lagrange elements [13], degenerated quadrilateral shell elements [14], triangular elements using the subdivision surface for the non-local interpolation [15] and quadrilateral elements satisfying the Kirchhoff-Love hypothesis at discrete nodes [2] have been developed. Numerical methods which can naturally construct the higher-order approximation and smooth discretization have been developed [16, 17].

The meshfree method can deal with not only the practical domain but also the parametric domain that is normally not considered in FEM. The physical domain is represented by scattered field nodes without considering meshes and elements, and the approximation, in which the local refinement can be flexibly implemented by directly adding field nodes, is based on the nodes within the support domain containing points of interest. The parametric domain can be treated in the same way as the physical domain. A variety of approaches have been developed for the meshfree method such as the smooth particle hydrodynamic (SPH) method [18], the element-free Galerkin (EFG) method [16, 19] and the reproducing kernel particle method (RKPM) [20, 21]. Comprehensive introductions of the meshfree method and recent development were presented in [22, 23] and monographs by Liu and Gu [24, 25]. Higher-order and smooth shape functions are convenient to construct in the meshfree method, which makes it more attractive for the analyses of thin shells. Krysl and Belytschko [19] firstly presented the analyses of Kirchhoff-Love shells using the EFG method which applied the moving least-squares (MLS) approximations [26]. Static and free vibration analyses of thin shells were further proposed using the EFG method [27], the RKPM method [28] and the radial basis approximation method [29]. Because of the nature of the meshfree method, crack propagation can be processed in a convenient manner without burdensome remeshing. The EFG method was employed to analyze static crack growth [30] and then the dynamic crack growth [31]. Analyses of thin shells for large deformation and dynamic fracture [32], and further improvements aiming to decrease the computational cost with the extrinsic basis were presented [33]. Large deformation analyses of thin shells were also implemented using the RKPM method [34, 35] and the local Kriging method [36].

The IGA method which integrates computer aided design (CAD) and computer aided engineering (CAE) adopts Non-Uniform Rational B-Splines (NURBS) basis functions to precisely represent geometries and approximate displacement fields [37]. The approximation can be treated in the physical domain and parametric domain for the IGA method. The applications of NURBS basis functions in the IGA method have been widely introduced [38, 39, 40, 41, 42, 43]. However, it is difficult to implement local refinement by using NURBS basis functions because of the tensor product. T-splines [44, 45] were developed and applied to the IGA method to improve the local refinement flexibility [46, 47] and solve trimmed surface problems [48]. A new local refinement strategy for the IGA method that can be flexibly implemented in the meshfree manner is proposed by introducing the equivalence between the meshfree shape functions and IGA basis functions [49].

Compared with other computational methods, the IGA method exhibits advantages in exact representation of the geometry and flexible construction of the higher-order and smooth basis functions, which makes it more perfect to analyze thin-shell structures. The middle surface of a thin shell is precisely represented by the NURBS basis functions so that the $C^1$ continuity is readily achieved. The linear and nonlinear analyses of Kirchhoff-Love shells were implemented by the IGA method in which NURBS basis functions were adopted to approximate displacement

variables [17, 50, 51]. The extended IGA (XIGA) was developed for the analyses of through-the-thickness cracks of thin shells [52, 53]. Because of complicated shell structures that consist of multiple patches, it is challenging to analyze these structures among patch interfaces [54]. The Nitsche's method was used to couple thin-shell patches and enforce geometrical continuities [55]. The large deformation analyses of thin shells using NURBS basis functions [56] and rational form of polynomial splines over hierarchical T-meshes (PHT-splines) basis functions [57, 58] were conducted. In these works, materials were treated as linearly elastic, and nonlinear material behaviors were considered in [59].

In order to preserve advantages of numerical methods and circumvent their disadvantages, different coupling approaches have been developed [60, 61, 62]. The coupling approaches normally utilize three subdomains, including the outer subdomain to obtain the boundary exactness, the interior subdomain to provide a flexible way to process problems such as the cracks and inclusions, and the coupling subdomain to realize smoothness. Belytschko et al. [62] proposed the finite element-element-free Galerkin coupling approach for elastodynamic problems. The coupling approach of the EFG method and the FEM utilized three subdomains: the meshfree subdomain to consider crack growth, the FEM subdomain to reduce computational cost and the coupling subdomain to achieve smoothness between the other two subdomains.

It is desirable to couple the IGA and meshfree methods because of such advantages as the exact geometry, the local refinement flexibility and the higher-order approximation. Two different types of coupling approaches of the IGA and meshfree methods are implemented in the parametric domain and physical domain, respectively. One approach coupling the IGA and the RKPM methods in the parametric domain was developed by Wang and Zhang [63]. The other approach for coupling two methods in the physical domain was developed by Valizadeh et al. [64] to couple the IGA and RKPM methods and by Rosolen and Arroyo [65] to couple the IGA method and the local maximum entropy meshfree method.

This paper aims to develop a coupling approach of the IGA and meshfree methods for the geometrically linear and nonlinear elastic analyses of thin-shell structures. The higher-order approximation can be achieved in the coupling approach so that the $C^1$ continuity of the displacement field is readily realized. The coupling approach utilizes three subdomains: the IGA subdomain for exact geometry representation, the meshfree subdomain for local refinement flexibility and the coupling subdomain for smoothness. The IGA subdomain and meshfree subdomain are respectively approximated by the NURBS basis functions and MLS shape functions, while the coupling subdomain is approximated by both functions based on the consistency conditions. The coupling approach can produce a higher convergence rate than the IGA and meshfree methods by implementing local refinement. The numerical results are verified by the reference solutions.

This paper is organized as follows. Section 2 introduces the meshfree and isogeometric approximations based on the MLS shape functions and the NURBS basis functions, respectively. Section 3 describes the coupling approach based on the consistency conditions. Section 4 presents the Kirchhoff-Love shell theory and shell discretization. Thin-shell benchmark problems are shown in Section 5 and the conclusions are drawn in Section 6.

## 2. Meshfree and isogeometric approximations

In this section, a brief description of the NURBS basis functions and the MLS shape functions is provided, which would be applied for the coupling approximation.

*2.1. MLS approximation*

The MLS approximation that was firstly proposed for data fitting and surface construction is employed to approximate the displacement field which can be calculated as follows [16]:

$$u^h(\boldsymbol{\xi}) = \sum_{J=1}^{\bar{m}} p_J(\boldsymbol{\xi})\,\bar{a}_J(\boldsymbol{\xi}) = \mathbf{p}^{\mathrm{T}}(\boldsymbol{\xi})\,\bar{\mathbf{a}}(\boldsymbol{\xi}), \tag{1}$$

where $\mathbf{p}(\boldsymbol{\xi})$ is the polynomial basis vector, $\bar{m}$ is the number of basis vectors and $\bar{\mathbf{a}}(\boldsymbol{\xi})$ is the vector of coefficients. A $p$th order polynomial basis vector in two dimensions is given as

$$\mathbf{p}(\boldsymbol{\xi}) = \left\{1, \xi, \eta, \xi^2, \xi\eta, \eta^2, \cdots, \xi^p, \cdots, \eta^p\right\}^{\mathrm{T}}. \tag{2}$$

The quadratic, cubic and quartic polynomial basis vectors are given as

$$\mathbf{p}(\boldsymbol{\xi}) = \begin{cases} \left\{1, \xi, \eta, \xi^2, \xi\eta, \eta^2\right\}^{\mathrm{T}} & (p=2) \\ \left\{1, \xi, \eta, \xi^2, \xi\eta, \eta^2, \xi^3, \xi^2\eta, \xi\eta^2, \eta^3\right\}^{\mathrm{T}} & (p=3) \\ \left\{1, \xi, \eta, \xi^2, \xi\eta, \eta^2, \xi^3, \xi^2\eta, \xi\eta^2, \eta^3, \xi^4, \xi^3\eta, \xi^2\eta^2, \xi\eta^3, \eta^4\right\}^{\mathrm{T}} & (p=4) \end{cases}. \tag{3}$$

The vector $\bar{\mathbf{a}}(\boldsymbol{\xi})$ in Eq. (1) is determined by minimizing the following weighted $L_2$ norm:

$$J = \sum_{I=1}^{N_{\mathrm{M}}} \widehat{W}(\boldsymbol{\xi} - \boldsymbol{\xi}_I)\left[\mathbf{p}^{\mathrm{T}}(\boldsymbol{\xi}_I)\,\bar{\mathbf{a}}(\boldsymbol{\xi}) - u_I\right]^2, \tag{4}$$

where $N_{\mathrm{M}}$ is the number of nodes within the support domain centered at the node $\boldsymbol{\xi}$ for which the weight function $\widehat{W}(\boldsymbol{\xi} - \boldsymbol{\xi}_I) \neq 0$, and $u_I$ denotes the nodal parameter of $u$ at $\boldsymbol{\xi} = \boldsymbol{\xi}_I$. The support domain is used to choose field nodes for the approximation and the circle domain is applied herein. The field nodes and support domains of a square plate are shown in Fig. 1.

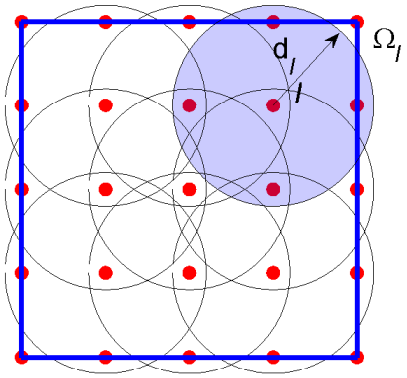


Figure 1: The discretization of a square plate: field nodes and support domains.

The derivative of $J$ with respect to $\bar{\mathbf{a}}(\boldsymbol{\xi})$ yields a set of linear equations as

$$\bar{\mathbf{A}}(\boldsymbol{\xi})\,\bar{\mathbf{a}}(\boldsymbol{\xi}) = \mathbf{B}\mathbf{U}, \tag{5}$$

where $\mathbf{U} = \{u_1, u_2, \cdots, u_{N_\mathrm{M}}\}^\mathrm{T}$ is the vector consisting of nodal parameters, and the weighted moment matrix $\bar{\mathbf{A}}(\boldsymbol{\xi})$ and the matrix $\mathbf{B}(\boldsymbol{\xi})$ are calculated as

$$\bar{\mathbf{A}}(\boldsymbol{\xi}) = \sum_{I=1}^{N_\mathrm{M}} \widehat{W}(\boldsymbol{\xi} - \boldsymbol{\xi}_I)\,\mathbf{p}(\boldsymbol{\xi}_I)\,\mathbf{p}^\mathrm{T}(\boldsymbol{\xi}_I), \tag{6}$$

$$\mathbf{B}(\boldsymbol{\xi}) = \left[\widehat{W}(\boldsymbol{\xi} - \boldsymbol{\xi}_1)\,p(\boldsymbol{\xi}_1) \quad \widehat{W}(\boldsymbol{\xi} - \boldsymbol{\xi}_2)\,p(\boldsymbol{\xi}_2) \quad \cdots \widehat{W}\left(\boldsymbol{\xi} - \boldsymbol{\xi}_{N_\mathrm{M}}\right) p\left(\boldsymbol{\xi}_{N_\mathrm{M}}\right)\right]. \tag{7}$$

The vector $\bar{\mathbf{a}}(\boldsymbol{\xi})$ is expressed as

$$\bar{\mathbf{a}}(\boldsymbol{\xi}) = \bar{\mathbf{A}}(\boldsymbol{\xi})^{-1}\mathbf{B}\mathbf{U}. \tag{8}$$

The MLS approximant can be obtained by substituting Eq. (8) into Eq. (1) as

$$u^h(\boldsymbol{\xi}) = \sum_{I=1}^{N_\mathrm{M}} \Psi_I(\boldsymbol{\xi})\,u_I(\boldsymbol{\xi}) = \boldsymbol{\Psi}(\boldsymbol{\xi})\,\mathbf{U}, \tag{9}$$

where the shape function $\Psi_I(\boldsymbol{\xi})$ is defined as

$$\Psi_I(\boldsymbol{\xi}) = \sum_{J=1}^{\bar{m}} \mathrm{p}_J(\boldsymbol{\xi})\left(\bar{A}^{-1}(\boldsymbol{\xi})\,B(\boldsymbol{\xi})\right)_{JI} = \mathbf{p}^\mathrm{T}(\boldsymbol{\xi})\left(\bar{\mathbf{A}}^{-1}\mathbf{B}\right)_I. \tag{10}$$

The weight function $\widehat{W}(\boldsymbol{\xi} - \boldsymbol{\xi}_I)$ in Eq. (4) determines the degree of smoothness of MLS shape functions. The quartic spline weight function which is chosen for the thin-shell analyses is given as

$$\widehat{W}(\boldsymbol{\xi} - \boldsymbol{\xi}_I) = \begin{cases} 1 - 6r^2 + 8r^3 - 3r^4 & (r \le 1) \\ 0 & (r > 1) \end{cases}, \quad r = \frac{|\boldsymbol{\xi} - \boldsymbol{\xi}_I|}{d^I_{max}}, \quad d^I_{max} = \lambda d_c, \tag{11}$$

where $d^I_{max}$ is the radius of the support domain centered at the node $\boldsymbol{\xi}_I$, $d_c$ denotes the average nodal spacing, and $\lambda$ represents the dimensionless size of the support domain. The optimized range of $\lambda$ is 2-4 [25].

The consistency condition means that any complete order of the polynomial can be exactly reproduced by the MLS approximation. The two-dimensional (2D) consistency condition is defined as

$$\sum_{I=1}^{N_\mathrm{M}} \Psi_I(\boldsymbol{\xi})\,\mathbf{p}(\boldsymbol{\xi}_I) = \mathbf{p}(\boldsymbol{\xi}). \tag{12}$$

### *2.2. Isogeometric approximation*

NURBS which are constructed by B-splines are commonly used in the CAD modeling and isogeometric approximation. A B-spline is a piecewise polynomial curve which is defined by the knot vector $\Xi = \left\{\xi_1, \xi_2, \cdots, \xi_{n+p+1}\right\}$, where $n$ is the number of control points, $p$ is the polynomial order and $\xi_i$ is the $i$th knot. The open knot vector in which the first and last knot values are repeated

with $p$+1 times is adopted here. The B-spline basis functions $N_{i,p}(\xi)$ can be defined recursively as

$$N_{i,0}(\xi) = \begin{cases} 1, & \xi_i \le \xi < \xi_{i+1} \\ 0, & \xi < \xi_i \text{or} \xi \ge \xi_{\text{i+1}} \end{cases} \qquad (p=0) \ , \tag{13}$$

$$N_{i,p}(\xi) = \frac{\xi - \xi_i}{\xi_{i+p} - \xi_i} N_{i,p-1}(\xi) + \frac{\xi_{i+p+1} - \xi}{\xi_{i+p+1} - \xi_{i+1}} N_{i+1,p-1}(\xi) \qquad (p \ge 1) \ . \tag{14}$$

A B-spline curve $\mathbf{C}(\xi)$ is obtained by taking the linear combination of basis functions $N_{i,p}(\xi)$ and control points $\mathbf{P}_i$:

$$\mathbf{C}(\xi) = \sum_{i=1}^{n} N_{i,p}(\xi) \mathbf{P}_i. \tag{15}$$

Two knot vectors are defined as $\Xi_1 = \left\{\xi_1, \xi_2, \cdots, \xi_{n+p+1}\right\}$ and $\Xi_2 = \left\{\eta_1, \eta_2, \cdots, \eta_{m+q+1}\right\}$. The B-spline surface can be computed based on the tensor product of these basis functions:

$$S(\xi, \eta) = \sum_{i=1}^{n} \sum_{j=1}^{m} N_{i,p}(\xi) M_{j,q}(\eta) \mathbf{P}_{i,j}, \tag{16}$$

where $N_{i,p}(\xi)$ and $M_{j,q}(\eta)$ are one-dimensional B-spline basis functions defined in Eqs. (13) and 14, and $\mathbf{P}_{i,j}$ are the corresponding control points.

A NURBS basis function is formulated as a linear combination of the B-spline basis functions and their corresponding weights. A NURBS surface with the $p$th and $q$th orders in bi-directions is defined as [66, 67]

$$S(\xi, \eta) = \sum_{i=1}^{n} \sum_{j=1}^{m} R_{i,j}(\xi, \eta) \mathbf{P}_{i,j}, \tag{17}$$

$$R_{i,j}(\xi, \eta) = R_I(\boldsymbol{\xi}) = \frac{N_{i,p}(\xi) M_{j,q}(\eta) w_{i,j}}{\sum_{\hat{i}=1}^{n} \sum_{\hat{j}=1}^{m} N_{\hat{i},p}(\xi) M_{\hat{j},q}(\eta) w_{\hat{i},\hat{j}}}. \tag{18}$$

## 3. The coupling approach of the IGA and meshfree methods

The consistency conditions of the meshfree method are expressed in Eq. (12). Similarly, the reproducing points for the IGA method are calculated by using the consistency conditions. The linear reproducing points are chosen as field nodes for the meshfree method herein.

### *3.1. Reproducing points for isogeometric basis functions*

The consistency conditions for univariate B-spline basis functions are defined as

$$\sum_{i=1}^{n} N_i^p(\xi) \mathbf{p}\left(\xi_i^{[l]}\right) = \mathbf{p}(\xi), \tag{19}$$

where $\mathbf{p}(\xi)=\left\{1,\xi,\xi^2,\cdots,\xi^p\right\}^{\mathrm{T}}$ denotes the one-dimensional polynomial basis vector. The one-dimensional reproducing point vector $\mathbf{p}\left(\xi_i^{[l]}\right)$ is defined as

$$\mathbf{p}\left(\xi_i^{[l]}\right)^{\mathrm{T}}=\left\{1,\xi_i^{[1]},\left(\xi_i^{[2]}\right)^2,\cdots,\left(\xi_i^{[p]}\right)^p\right\}, \tag{20}$$

and the reproducing points $\xi_i^{[l]}\,(l=1,2,\cdots,p)$ for the monomial $\xi^l$ are calculated as [63]

$$\xi_i^{[l]}=\sqrt[l]{\frac{S_p^l\left[G_{i+1}^{i+p}\right]}{C_p^l}}\quad,\quad C_p^l=\frac{p!}{l!\,(p-l)!}, \tag{21}$$

where $G_{i+1}^{i+p}=\left\{\xi_{i+1},\xi_{i+2},\cdots,\xi_{i+p}\right\}$ is the knot vector, the operator $S_p^l$ means selecting $l$ knots from $G$ and multiplying them as one term, and then adding all the terms together. When $p$ equals 2, the reproducing points $\xi_i^{[l]}$ can be calculated as [63]

$$\xi_i^{[l]}=\begin{cases}\xi_i^{[1]}=\frac{\xi_{i+1}+\xi_{i+2}}{2}\\ \xi_i^{[2]}=\sqrt{\xi_{i+1}\xi_{i+2}}\end{cases}. \tag{22}$$

For 2D basis functions, the following consistency conditions can be readily obtained based on the tensor product of B-spline basis functions:

$$\sum_{i=1}^{n}\sum_{j=1}^{m}N_{i,p}(\xi)M_{j,q}(\eta)\left(\xi_i^{[\alpha]}\right)^{\alpha}\left(\eta_j^{[\beta]}\right)^{\beta}=\xi^{\alpha}\eta^{\beta}\quad,\quad(\alpha+\beta\le p+q)\ . \tag{23}$$

Eq. (23) can be simplified as

$$\sum_{I=1}^{N_{\mathrm{B}}}N_I^{pq}(\boldsymbol{\xi})\,\mathbf{p}\left(\boldsymbol{\xi}_I^{[l]}\right)=\mathbf{p}(\boldsymbol{\xi}), \tag{24}$$

where $N_I^{pq}(\boldsymbol{\xi})=N_{i,p}(\xi)M_{j,q}(\eta)$, $N_{\mathrm{B}}$ represents the number of basis functions and $\mathbf{p}\left(\boldsymbol{\xi}_I^{[l]}\right)$ is the 2D reproducing point vector:

$$\mathbf{p}\left(\boldsymbol{\xi}_I^{[l]}\right)^{\mathrm{T}}=\left\{1,\xi_I^{[1]},\eta_I^{[1]},\left(\xi_I^{[2]}\right)^2,\xi_I^{[1]}\eta_I^{[1]},\left(\eta_I^{[2]}\right)^2,\cdots,\left(\xi_I^{[p]}\right)^p,\cdots,\left(\eta_I^{[q]}\right)^q\right\}, \tag{25}$$

where $\boldsymbol{\xi}_I^{[l]}$ denote the 2D reproducing points.

### *3.2. Coupling approximation*

Based on the IGA-RKPM coupling approach in which the reproducing kernel approximation is equivalent to the MLS approximation when monomial basis functions are applied, the NURBS basis functions and the MLS shape functions are coupled in the parametric domain [63]. The parametric domain is divided into the IGA subdomain $\Omega_{\xi}^{\mathrm{IGA}}$, the meshfree subdomain $\Omega_{\xi}^{\mathrm{MF}}$ and the coupling subdomain $\Omega_{\xi}^{\mathrm{CP}}$, and their corresponding physical subdomains are represented by $\Omega^{\mathrm{IGA}}$, $\Omega^{\mathrm{MF}}$ and $\Omega^{\mathrm{CP}}$, respectively. The IGA subdomain is responsible for the outer part that contains the

boundary, and the meshfree subdomain is responsible for the interior part which will be desirable for cracks and inclusions. Other layouts of these subdomains have been presented in [63].

The displacement $u_{\mathrm{I}}(\mathbf{x})$ can be approximated based on the coupling approach as follows:

$$u_I(\mathbf{x}) = \sum_{I=1}^{N_{\mathrm{S}}} \Phi_I(\boldsymbol{\xi})\, u_I, \tag{26}$$

where $\mathbf{x} = [x, y, z]^T$ is considered for the thin-shell analysis, $N_{\mathrm{S}}$ is the number of shape functions, $u_I$ is the coefficient related to the control point and $\Phi_I(\boldsymbol{\xi})$ is the shape function given as

$$\Phi_I(\boldsymbol{\xi}) = \begin{cases} R_I(\boldsymbol{\xi}) & \boldsymbol{\xi}_I \in \Omega_{\xi}^{\mathrm{IGA}} \\ R_I(\boldsymbol{\xi}) + \Psi_I^{\mathrm{CP}}(\boldsymbol{\xi}) & \boldsymbol{\xi}_I \in \Omega_{\xi}^{\mathrm{CP}} \\ \Psi_I(\boldsymbol{\xi}) & \boldsymbol{\xi}_I \in \Omega_{\xi}^{\mathrm{MF}} \end{cases}, \tag{27}$$

where $\Psi_I(\boldsymbol{\xi})$ and $R_I(\boldsymbol{\xi})$ represent the MLS shape function and the NURBS basis function, respectively.

The coupling shape function $\Psi_J^{\mathrm{CP}}(\boldsymbol{\xi})$ can be obtained based on the consistency conditions expressed in Eqs. (12) and (24). The NURBS basis function is treated as a constant in the coupling subdomain. The $p$th order consistency condition is defined as

$$\sum_{I=1}^{N_{\mathrm{S}}} \Phi_I(\boldsymbol{\xi})\, \mathbf{p}\left(\boldsymbol{\xi}_I^{[l]}\right) = \sum_{J=1}^{N_{\mathrm{M}}} \Psi_J^{\mathrm{CP}}(\boldsymbol{\xi})\, \mathbf{p}\left(\boldsymbol{\xi}_J^{[l]}\right) + \sum_{I=1}^{N_{\mathrm{B}}} R_I(\boldsymbol{\xi})\, \mathbf{p}\left(\boldsymbol{\xi}_I^{[l]}\right) = \mathbf{p}(\boldsymbol{\xi}), \tag{28}$$

where $\mathbf{p}\left(\boldsymbol{\xi}_I^{[l]}\right)$ is the reproducing point vector defined in Eq. (25).

The meshfree shape function $\Psi_J^{\mathrm{CP}}(\boldsymbol{\xi})$ can be expressed in the same way as in Eq. (10):

$$\Psi_J^{\mathrm{CP}}(\boldsymbol{\xi}) = \mathbf{p}^{\mathrm{T}}\left(\boldsymbol{\xi}_J^{[l]}\right) \mathbf{c}(\boldsymbol{\xi})\, \widehat{W}\left(\boldsymbol{\xi} - \boldsymbol{\xi}_J^{[1]}\right). \tag{29}$$

The following expression can be obtained by substituting Eq. (29) into Eq. (28):

$$\mathbf{c}(\boldsymbol{\xi}) = \bar{\mathbf{C}}^{-1}(\boldsymbol{\xi})\left[\mathbf{p}(\boldsymbol{\xi}) - \mathbf{q}(\boldsymbol{\xi})\right], \tag{30}$$

with

$$\bar{\mathbf{C}}(\boldsymbol{\xi}) = \sum_{J=1}^{N_{\mathrm{M}}} \mathbf{p}\left(\boldsymbol{\xi}_J^{[l]}\right) \mathbf{p}^T\left(\boldsymbol{\xi}_J^{[l]}\right) \widehat{W}\left(\boldsymbol{\xi} - \boldsymbol{\xi}_J^{[1]}\right), \tag{31}$$

$$\mathbf{q}(\boldsymbol{\xi}) = \sum_{I=1}^{N_{\mathrm{B}}} R_I(\boldsymbol{\xi})\, \mathbf{p}\left(\boldsymbol{\xi}_I^{[l]}\right). \tag{32}$$

The meshfree shape function $\Psi_J^{\mathrm{CP}}(\boldsymbol{\xi})$ in the coupling subdomain is obtained as

$$\Psi_J^{\mathrm{CP}}(\boldsymbol{\xi}) = \mathbf{p}^T\left(\boldsymbol{\xi}_J^{[l]}\right) \bar{\mathbf{C}}^{-1}(\boldsymbol{\xi})\left[\mathbf{p}(\boldsymbol{\xi}) - \mathbf{q}(\boldsymbol{\xi})\right] \widehat{W}\left(\boldsymbol{\xi} - \boldsymbol{\xi}_J^{[1]}\right). \tag{33}$$

Eqs. (10), (18) and (33) constitute basis functions of the coupling approximation.

A 2D problem is provided herein to demonstrate the modeling steps. Two knot vectors, $\Xi_1 = \left\{0,0,0,\frac{1}{8},\frac{2}{8},\frac{3}{8},\frac{4}{8},\frac{5}{8},\frac{6}{8},\frac{7}{8},1,1,1\right\}$ and $\Xi_2 = \left\{0,0,0,\frac{1}{8},\frac{2}{8},\frac{3}{8},\frac{4}{8},\frac{5}{8},\frac{6}{8},\frac{7}{8},1,1,1\right\}$, are defined to construct NURBS basis functions. Based on Eq. (22), the linear and quadratic reproducing points of two directions are calculated as

$$\xi_I^{[1]} = \eta_I^{[1]} = \left\{0, \frac{1}{16}, \frac{3}{16}, \frac{5}{16}, \frac{7}{16}, \frac{9}{16}, \frac{11}{16}, \frac{13}{16}, \frac{15}{16}, 1\right\}, \tag{34}$$

$$\xi_I^{[2]} = \eta_I^{[2]} = \left\{0, 0, \sqrt{\frac{1}{32}}, \sqrt{\frac{3}{32}}, \sqrt{\frac{3}{16}}, \sqrt{\frac{5}{16}}, \sqrt{\frac{15}{32}}, \sqrt{\frac{21}{32}}, \sqrt{\frac{7}{8}}, 1\right\}. \tag{35}$$

The shape functions can be obtained according to Eq. (27), as shown in Fig. 2. It is seen that the smooth transition is achieved among the IGA subdomain, coupling subdomain and meshfree subdomain. Fig. 3 shows the discretization of the circle geometry in the parametric domain and physical domain by using the coupling approximation.

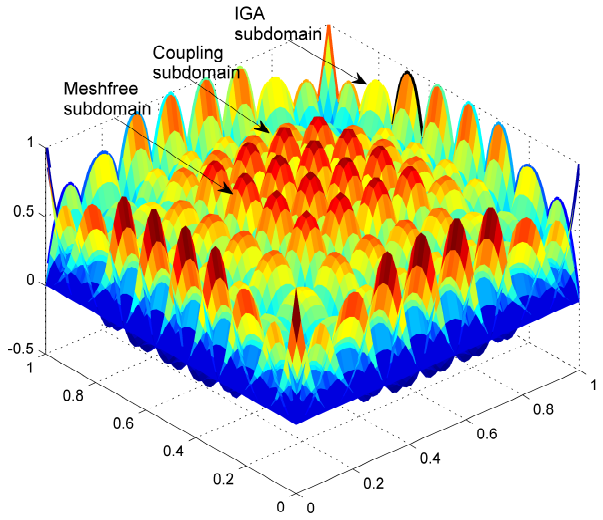


Figure 2: Quadratic shape functions of the 2D coupling approximation.

### *3.3. Local refinement strategy*

The advantage of local refinement flexibility in the meshfree method is preserved in the coupling approach. Local refinement is implemented within the meshfree subdomain. Take the local refinement strategy in 2D as an example: each background mesh is subdivided into 4 submeshes and 5 nodes are inserted. The further refinement can be treated in the same way until the stopping criterion is met.

Fig. 4 shows the refinement processes of the first three levels. The original nodes and newly inserted nodes are denoted by the solid circle and hollow circle, respectively. The initial mesh 1 is subdivided into meshes 2, 3, 4 and 5 in the second level of refinement. In the third level of refinement, the mesh 5 is subdivided into meshes 6, 7, 8 and 9. The new support sizes are

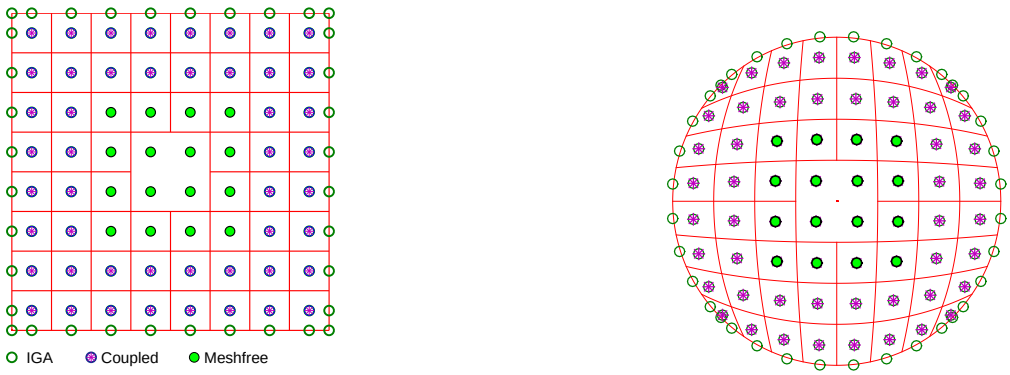


(a) (b)

Figure 3: The 2D coupling discretization: (a) the parametric domain and (b) the physical domain.

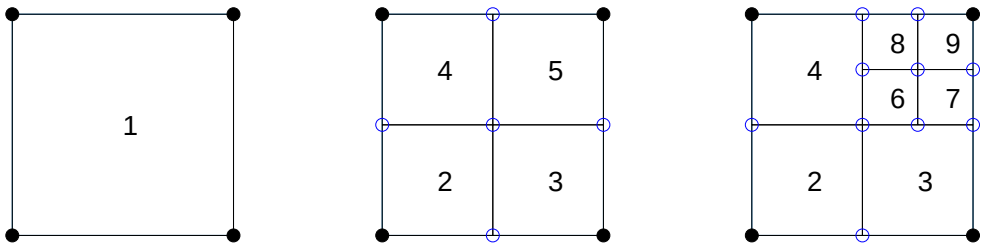


(a) (b) (c)

Figure 4: The local refinement strategy: (a) the initial mesh, (b) the mesh in the second level and (c) the mesh in the third level.

calculated for the inserted nodes to improve the MLS approximation between the coarse and fine meshes [71].

## 4. Thin-shell theory

### *4.1. Kinematics of the shell*

In the Kirchhoff-Love theory, the transverse shear deformations are neglected and transverse shear strains are zero. Another assumption is that a vector normal to the middle surface remains normal to the deformed middle surface. The mid-surface shell model is analyzed for the thin-shell structures.

The position of a material point in the reference configuration is described as

$$\mathbf{X}_0\left(\xi^1,\xi^2,\xi^3\right)=\boldsymbol{\varphi}_0\left(\xi^1,\xi^2\right)+\xi^3\mathbf{A}_3\left(\xi^1,\xi^2\right), \tag{36}$$

where $\xi^1,\xi^2\in\mathbb{R}^2$ are convective curvilinear coordinates, $-0.5t\leq\xi^3\leq 0.5t$ denotes the thickness of the material point, $t$ is the thickness, $\mathbf{A}_3$ is the normal vector of the middle surface and $\boldsymbol{\varphi}_0$ is the position of a material point on the middle surface. Similarly, the position of a material point $\mathbf{x}$ in the deformed configuration can be expressed by $\boldsymbol{\varphi}$ and $\mathbf{a}_3$. The displacement of a material point on the middle surface is calculated as

$$\mathbf{u}\left(\xi^1,\xi^2\right)=\boldsymbol{\varphi}\left(\xi^1,\xi^2\right)-\boldsymbol{\varphi}_0\left(\xi^1,\xi^2\right). \tag{37}$$

Based on the Kirchhoff-Love theory, the Green-Lagrange strain tensor is expressed as

$$\mathbf{E}=E_{\alpha\beta}\mathbf{G}^{\alpha}\otimes\mathbf{G}^{\beta}\ ,\quad E_{\alpha\beta}=\left(\varepsilon_{\alpha\beta}+\xi^3\kappa_{\alpha\beta}\right)\quad(\alpha,\beta=1,2)\ , \tag{38}$$

where $\mathbf{G}^{\alpha}$ and $\mathbf{G}^{\beta}$ are the contravariant basis vectors presented in Appdendix A, and $\varepsilon_{\alpha\beta}$ denotes the membrane strain and $\kappa_{\alpha\beta}$ represents the change of curvature [11, 68]:

$$\varepsilon_{\alpha\beta}=\frac{1}{2}\left(\mathbf{a}_{\alpha}\cdot\mathbf{a}_{\beta}-\mathbf{A}_{\alpha}\cdot\mathbf{A}_{\beta}\right), \tag{39}$$

$$\kappa_{\alpha\beta}=\mathbf{A}_{\alpha,\beta}\cdot\mathbf{A}_3-\mathbf{a}_{\alpha,\beta}\cdot\mathbf{a}_3, \tag{40}$$

with $\mathbf{a}_{\alpha}$, $\mathbf{A}_{\alpha}$, $\mathbf{a}_{\alpha,\beta}$ and $\mathbf{A}_{\alpha,\beta}$ introduced in Appendix A.

### *4.2. Equilibrium equations of thin shells*

Based on the principle of virtual work, the total sum of the internal and external work equals zero:

$$\delta W=\delta W_{\text{int}}+\delta W_{\text{ext}}=0. \tag{41}$$

The internal virtual work $\delta W_{\text{int}}$ is described as

$$\delta W_{\text{int}}=-\int_V\delta\mathbf{E}:\mathbf{S}\mathrm{d}V, \tag{42}$$

where $\delta$ represents a variation, and $\mathbf{S}$ is the second Piola-Kirchhoff stress.

The internal virtual work is integrated through the thickness [69]:

$$-\int_V \delta\mathbf{E} : \mathbf{S}\mathrm{d}V = -\int_A (\mathbf{n} : \delta\boldsymbol{\varepsilon} + \mathbf{m} : \delta\boldsymbol{\kappa})\mathrm{d}A, \tag{43}$$

where the membrane stresses $\mathbf{n} = t\mathbf{C}\boldsymbol{\varepsilon}$ and the bending stresses $\mathbf{m} = \frac{t^3}{12}\mathbf{C}\boldsymbol{\kappa}$ are expressed by the Voigt's notation, d$A$ is the differential area of the middle surface given as

$$\mathrm{d}A = \bar{j}_0 d\xi^1 d\xi^2 \ , \quad \bar{j}_0 = \|\mathbf{A}_1 \times \mathbf{A}_2\|, \tag{44}$$

with

$$\mathbf{C} = \frac{E}{1-\nu^2}\begin{bmatrix} \left(A^{11}\right)^2 & \nu A^{11}A^{22} + (1-\nu)\left(A^{12}\right)^2 & A^{11}A^{12} \\ \vdots & \left(A^{22}\right)^2 & A^{22}A^{12} \\ \text{Sym.} & \cdots & \frac{1}{2}\left[(1-\nu)A^{11}A^{22} + (1+\nu)\left(A^{12}\right)^2\right] \end{bmatrix}, \tag{45}$$

where $E$ is the Young's modulus, $\nu$ is the Poisson's ratio and the contravariant metric coefficients $A^{\alpha\beta}$ are calculated in Appendix A.

The first derivative of the virtual work yields the residual force vector $\mathbf{R}$:

$$\mathbf{R} = \left(\frac{\partial W_{\text{int}}}{\partial u_r} + \frac{\partial W_{\text{ext}}}{\partial u_r}\right) = F_r^{\text{int}} + F_r^{\text{ext}}. \tag{46}$$

The second derivative of the virtual work yields the internal stiffness $K_{rs}^{\text{int}}$:

$$K_{rs}^{\text{int}} = \int_A \left(\frac{\partial \mathbf{n}}{\partial u_s} : \frac{\partial \boldsymbol{\varepsilon}}{\partial u_r} + \mathbf{n} : \frac{\partial^2 \boldsymbol{\varepsilon}}{\partial u_r \partial u_s} + \frac{\partial \mathbf{m}}{\partial u_s} : \frac{\partial \boldsymbol{\kappa}}{\partial u_r} + \mathbf{m} : \frac{\partial^2 \boldsymbol{\kappa}}{\partial u_r \partial u_s}\right)\mathrm{d}A. \tag{47}$$

For the linear deformation, the stiffness matrix can be reduced as

$$\bar{K}_{rs}^{\text{int}} = \int_A \left(\frac{\partial \mathbf{n}}{\partial u_s} : \frac{\partial \boldsymbol{\varepsilon}}{\partial u_r} + \frac{\partial \mathbf{m}}{\partial u_s} : \frac{\partial \boldsymbol{\kappa}}{\partial u_r}\right)\mathrm{d}A. \tag{48}$$

### *4.3. Discretization of thin shells*

The deformed and undeformed middle surfaces can be defined in the same way as the displacement represented by the shape function $\Phi_I(\boldsymbol{\xi})$ in Eq. (27) as

$$\varphi\left(\xi^1, \xi^2\right) = \sum_{I=1}^{N_{\text{S}}} \Phi_I(\boldsymbol{\xi})\, p_I^* \ , \quad \varphi_0\left(\xi^1, \xi^2\right) \ = \sum_{I=1}^{N_{\text{S}}} \Phi_I(\boldsymbol{\xi})\, p_I, \tag{49}$$

where $p_I, p_I^* \in \mathbb{R}^3$ are control points in the initial and deformed configurations, respectively.

Based on the linearized kinematics introduced in Appendix B, the membrane and bending

strains can be expressed in the Voigt's notation as [15]

$$\boldsymbol{\varepsilon} = \begin{bmatrix} \varepsilon_{11} \\ \varepsilon_{22} \\ 2\varepsilon_{12} \end{bmatrix} = \sum_{I=1}^{N_S} \mathbf{B}_n^I u_I \ , \quad \boldsymbol{\kappa} = \begin{bmatrix} \kappa_{11} \\ \kappa_{22} \\ 2\kappa_{12} \end{bmatrix} = \sum_{I=1}^{N_S} \mathbf{B}_m^I u_I, \tag{50}$$

where the membrane matrix $\mathbf{B}_n^I$ and the bending matrix $\mathbf{B}_m^I$ are expressed as

$$\mathbf{B}_n^I = \begin{bmatrix} (\mathbf{A}_1 \Phi_{I,1})^T \\ (\mathbf{A}_2 \Phi_{I,2})^T \\ (\mathbf{A}_1 \Phi_{I,2} + \mathbf{A}_2 \Phi_{I,1})^T \end{bmatrix} \ , \quad \mathbf{B}_m^I = \begin{bmatrix} (\mathbf{b}_{m11}^I)^T \\ (\mathbf{b}_{m22}^I)^T \\ (2\mathbf{b}_{m12}^I)^T \end{bmatrix} \ , \tag{51}$$

with

$$\begin{aligned} \mathbf{b}_{m\alpha\beta}^I = \mathbf{A}_{\alpha,\beta} \cdot \mathbf{A}_3 \tfrac{1}{j_0} \left[ \Phi_{I,1} (\mathbf{A}_2 \times \mathbf{A}_3) + \Phi_{I,2} (\mathbf{A}_3 \times \mathbf{A}_1) \right] \\ - \tfrac{1}{j_0} \left[ \Phi_{I,1} \left( \mathbf{A}_2 \times \mathbf{A}_{\alpha,\beta} \right) + \Phi_{I,2} \left( \mathbf{A}_{\alpha,\beta} \times \mathbf{A}_1 \right) \right] - \Phi_{I,\alpha\beta} \mathbf{A}_3 \end{aligned} \ . \tag{52}$$

The global stiffness matrices of the nonlinear deformation and linear deformation are obtained by substituting $\boldsymbol{\varepsilon}$, $\boldsymbol{\kappa}$, $\mathbf{n}$, $\mathbf{m}$ and their derivatives that are presented in Appendix C into Eqs. (47) and (48). The linearized systems are given as

$$\mathbf{K}_{\mathrm{rs}}^{\mathrm{int}} \Delta \mathbf{u} = \mathbf{R}, \tag{53}$$

$$\bar{\mathbf{K}}_{\mathrm{rs}}^{\mathrm{int}} \mathbf{u} = \mathbf{F}^{\mathrm{ext}}. \tag{54}$$

The nonlinear deformation $\Delta \mathbf{u}$ is obtained based on the Newton-Raphson method [70] and the linear one can be directly calculated by Eq. (54).

## 5. Numerical examples

In this section, the coupling approach is applied to solve thin-shell benchmarks containing linear and nonlinear deformation. For the MLS approximation, the weight function is the quartic spline with support sizes 2, 3 and 4 for the quadratic, cubic and quartic approximations, respectively. The 4 x 4 gauss quadrature rule is applied for the integration in the coupling approximation.

### *5.1. Linear deformation*

The benchmark problems proposed by Belytschko et al. [14] that contain a pinched cylindrical shell with rigid diaphragms, a Scordelis-Lo roof and a hemispherical shell are analyzed by using the coupling approach. Local refinement is implemented by directly inserting meshfree nodes around the point loadings where stress concentrations occur.

The errors in the displacement and strain energy which are respectively denoted by $err_{disp}$ and $err_{ener}$ are calculated as

$$err_{disp} = \frac{\sqrt{\int_\Omega (\mathbf{u} - \mathbf{u}_{ect}) \cdot (\mathbf{u} - \mathbf{u}_{ect}) \, d\Omega}}{\sqrt{\int_\Omega \mathbf{u}_{ect} \cdot \mathbf{u}_{ect} d\Omega}}, \tag{55}$$

$$err_{ener} = \frac{\sqrt{\int_{\Omega} \mathbf{E}^T(\mathbf{u}-\mathbf{u}_{ect}) : \mathbf{C} : \mathbf{E}(\mathbf{u}-\mathbf{u}_{ect})\, d\Omega}}{\sqrt{\int_{\Omega} \mathbf{E}^T(\mathbf{u}_{ect}) : \mathbf{C} : \mathbf{E}(\mathbf{u}_{ect})\, d\Omega}}, \tag{56}$$

where $\mathbf{u}_{ect}$ are the estimated exact displacements. Since there are no exact results for these shell problems, the higher-order NURBS approximation ($p = q = 9$) is applied to calculate $\mathbf{u}_{ect}$ and estimate the error norms.

### *5.1.1. Pinched cylindrical shell*

A cylindrical shell which is supported by fixed diaphragms at both ends is subjected to two opposite point loadings $P$ = 1 N, as shown in Fig. 5(a). The geometry parameters are the radius $R$ = 300 mm, the length $L$ = 600 mm and the thickness $t$ = 1 mm. The material properties are the Young's modulus $E = 3\times10^6$ N/mm$^2$ and the Poisson's ratio $\nu = 0.3$. One eighth of the cylindrical shell is modeled because of the symmetry (Fig. 5(b)).

Fig. 6(a) shows the contour plots of displacements in the deformed configuration with the scaling factor of $1\times10^7$. The results converge to the analytical solution $1.8248\times10^{-5}$ mm as global refinement is conducted [14]. The errors in the strain energy using the quadratic shape function are shown in Fig. 6(b). The coupling approach realizes the exact boundaries and meanwhile converges faster than the meshfree method. Moreover, the coupling approach with local refinement produces a higher convergence rate than global refinement.

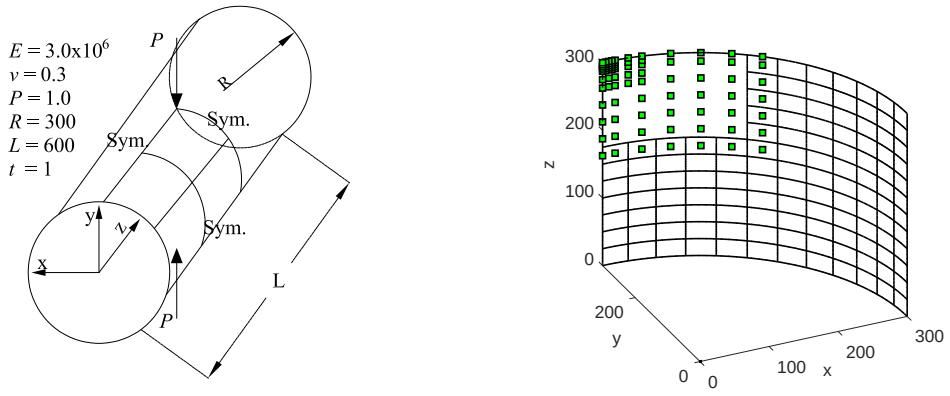


(a) (b)

Figure 5: The pinched cylindrical shell with rigid diaphragms: (a) the geometry and (b) the locally refined meshes in the physical domain.

### *5.1.2. Scordelis-Lo roof*

A Scordelis-Lo roof, a section of the cylindrical shell supported by rigid diaphragms, is considered. The roof is subjected to the uniform gravity load $P$ = 90 N, as shown in Fig. 7. The geometry

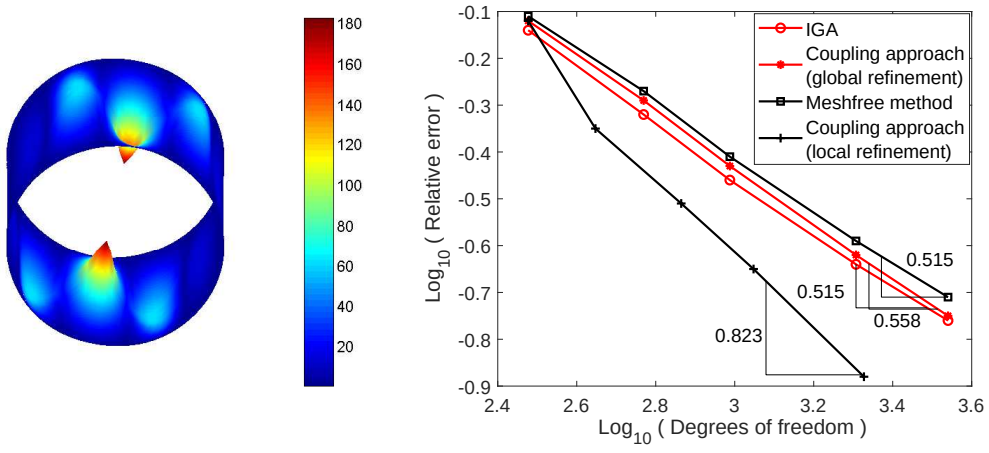


(a) (b)

Figure 6: (a) The contour plots of displacements in the deformed configuration (scaling factor of $1\times10^7$) and (b) the errors in the strain energy of the pinched cylindrical shell.

parameters are the length $L = 50$ mm, the radius $R = 25$ mm and the thickness $t = 0.25$ mm. The material properties are the Young's modulus $E = 4.32\times10^8$ N/mm$^2$ and the Poisson's ratio $\nu = 0.0$.

Fig. 8(a) shows the contour plots of displacements in the deformed configuration with the scaling factor of 10. Fig. 8(b) shows the errors in the displacement using the quadratic approximation. The coupling approach with local refinement achieves a higher convergence rate than global refinement. Moreover, the coupling approach (with local refinement) performs better than the IGA method (with global refinement) when the meshes are refined. The force and moment resultants are shown in Fig. 9.

### *5.1.3. Hemispherical shell*

A hemispherical shell subjected to two opposite point forces $F = 2$ N is considered (Fig. 10(a)). The geometry parameters are the radius $R = 10$ mm and the thickness $t = 0.04$ mm. The material properties include the Young's modulus $E = 6.825\times10^7$ N/mm$^2$ and the Poisson's ratio $\nu = 0.3$. The locally refined meshes for one quarter of the hemispherical shell are plotted in the physical domain (Fig. 10(b)).

Fig. 11(a) shows the contour plots of displacements in the deformed configuration. Fig. 11(b) shows the errors in the strain energy using the quadratic approximation. The coupling approach (with global refinement) achieves the same convergence rate as the IGA method (with global refinement) when meshes are refined. Furthermore, the coupling approach with local refinement converges faster than global refinement.

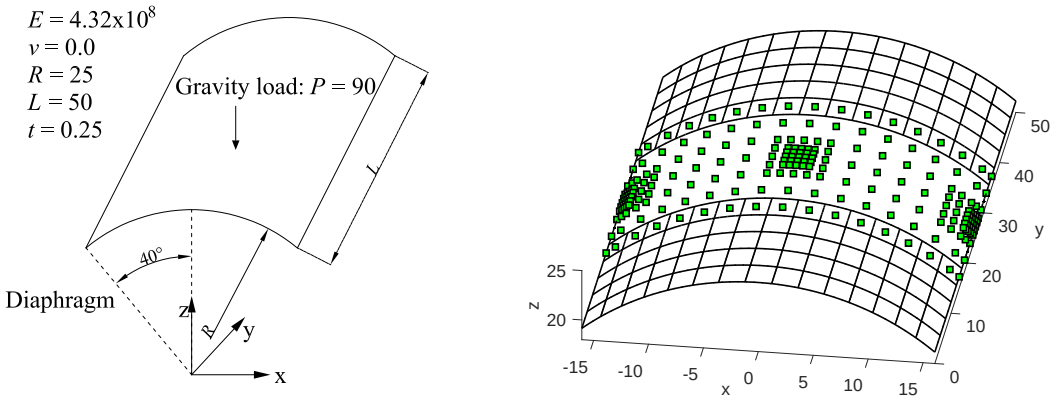


(a) (b)

Figure 7: (a) The geometry and material parameters of the Scordelis-Lo roof and (b) the meshes with local refinement.

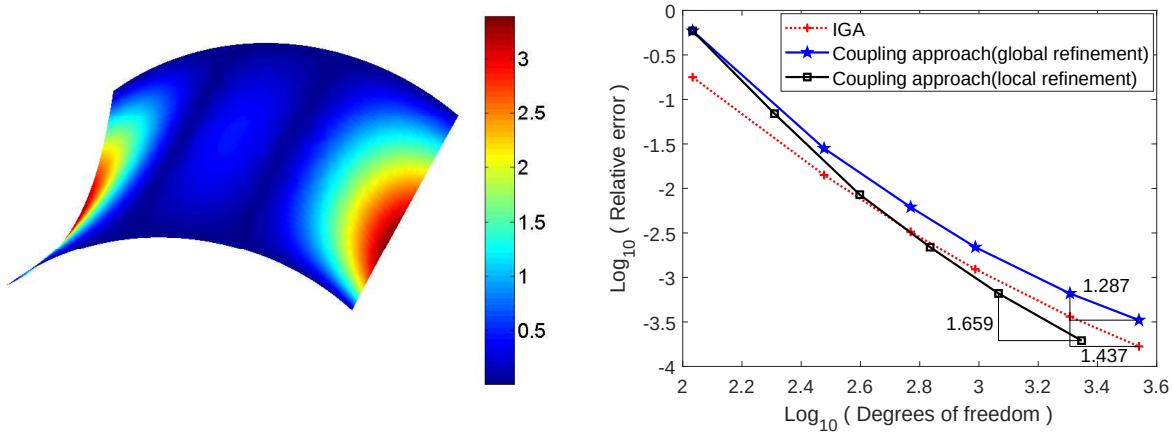


(a) (b)

Figure 8: (a) The contour plots of displacements in the deformed configuration (scaling factor of 10) and (b) the errors in the displacement of the Scordelis-Lo roof.

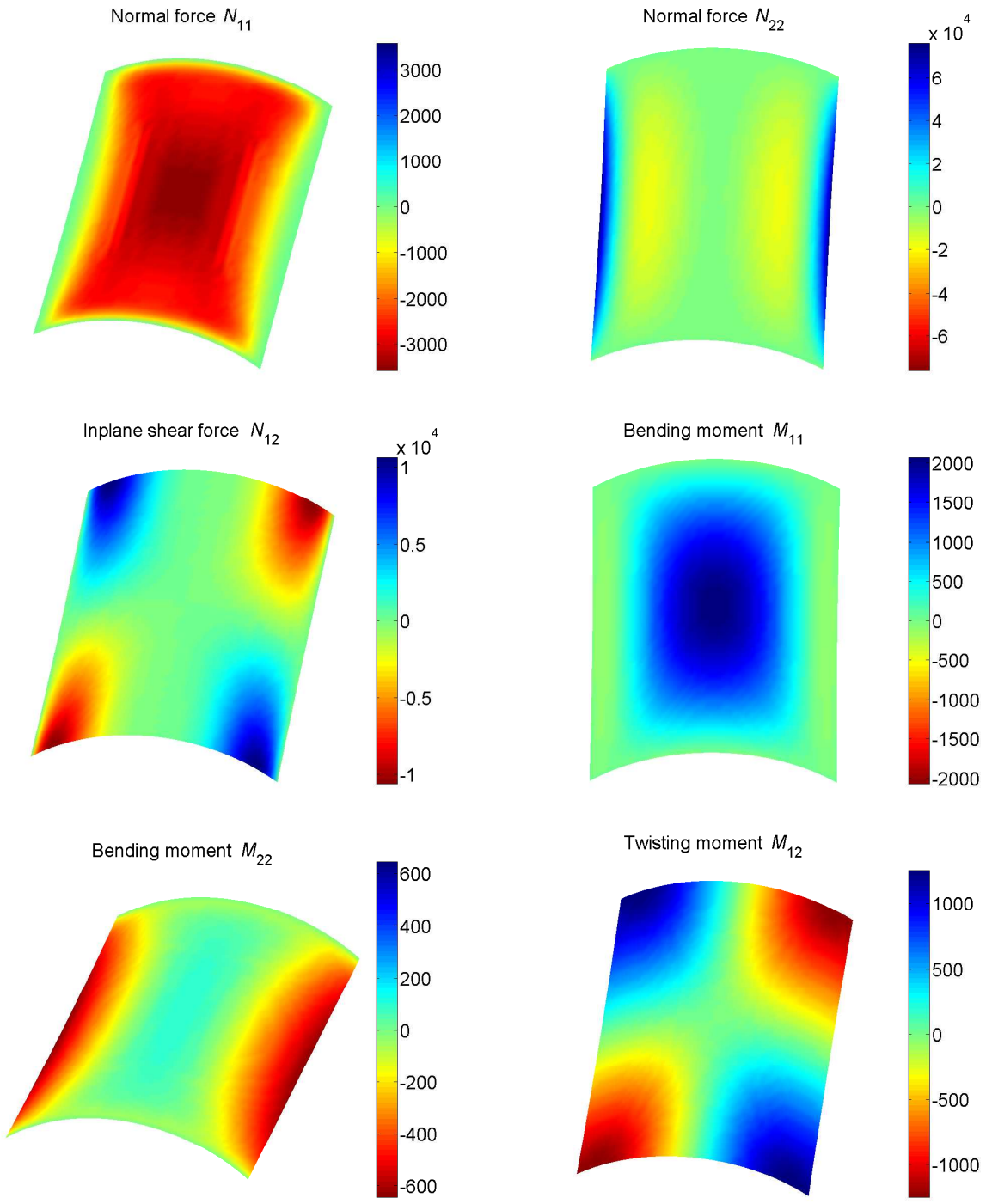


Figure 9: The contour plots of the force and moment resultants of the Scordelis-Lo roof.

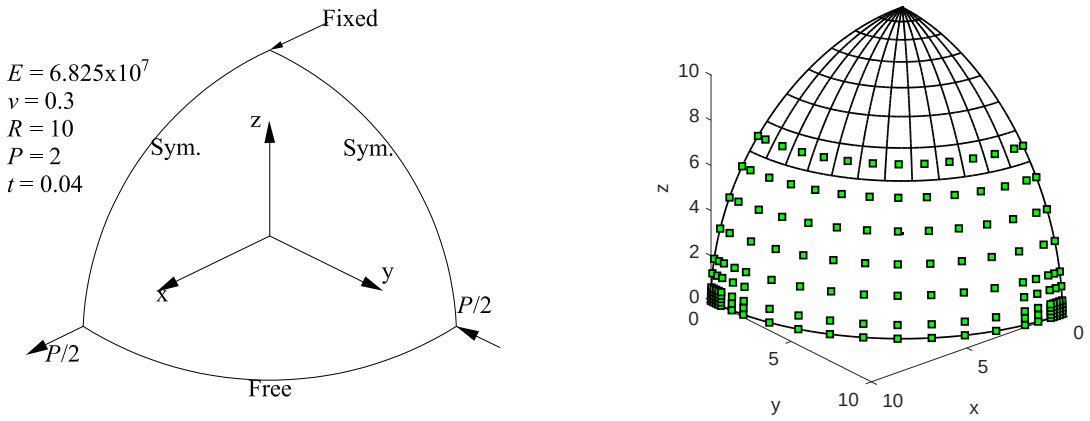


(a) (b)

Figure 10: The hemispherical shell: (a) one quarter of the geometry and (b) the locally refined meshes.

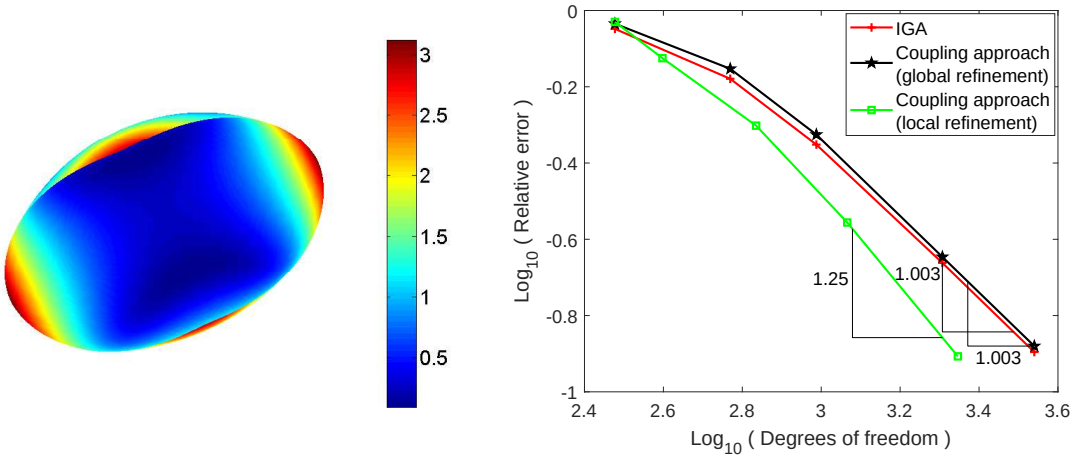


(a) (b)

Figure 11: (a) The contour plots of displacements in the deformed configuration (scaling factor of 30) and (b) the errors in the strain energy of the hemispherical shell.

### 5.2. *Nonlinear deformation*

The benchmark problems including a cantilever plate, a hemispherical shell, a pinched cylindrical shell and an open-ended cylindrical shell are analyzed by the coupling approach. The coupling approximation regards the outer part of geometry as the IGA subdomain and the interior part of the geometry as the meshfree subdomain.

#### 5.2.1. *Cantilever plate*

A cantilever plate subjected to the shear force $P = 4$ N is considered, as shown in Fig. 12(a). The geometry parameters are the length $L = 10$ mm, the thickness $t = 0.1$ mm and the width $b = 1$ mm. The material properties include the Young's modulus $E = 1.2\times10^6$ N/mm$^2$ and the Poisson's ratio $\nu = 0.3$. The quadratic basis function is used to approximate the displacement variables. The shear force is equally applied in 40 load steps.

Fig. 12(b) shows the contour plots of displacements at different load steps. Fig. 13 shows the displacements at the end of the cantilever. The numerical results are consistent with the reference solutions [72], demonstrating the accuracy of the geometrically nonlinear analysis with the coupling approach.

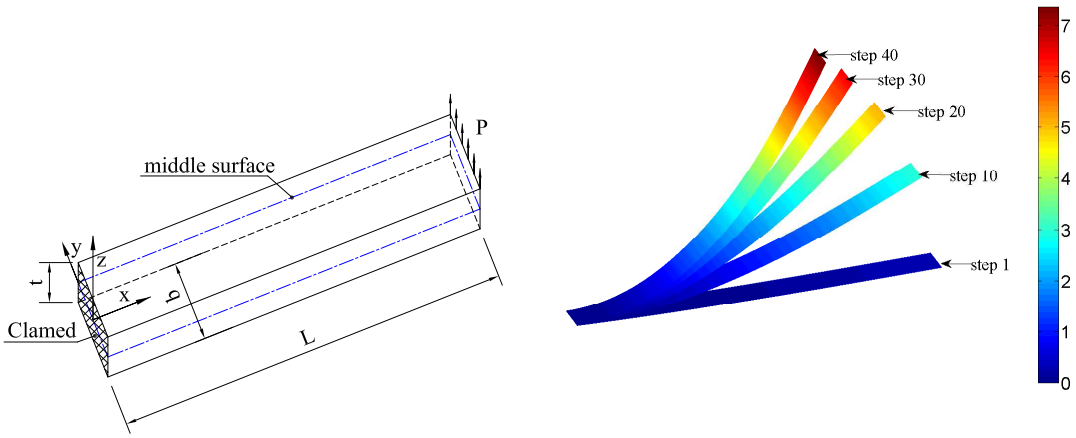


(a) (b)

Figure 12: The cantilever plate subjected to a shear force: (a) the geometry and (b) the contour plots of displacements at several load steps.

#### 5.2.2. *Hemispherical shell*

A hemispherical shell with a 18° hole at the top loaded by equal but opposite forces $P = 400$ N is considered (Fig. 14(a)). The geometry parameters include the radius $R = 10$ mm and the thickness $t = 0.04$ mm. The material properties are the Young's modulus $E = 6.825\times10^7$ N/mm$^2$ and the Poisson's ratio $\nu = 0.3$. The quadratic and cubic basis functions are adopted for the coupling approximation and 40 equal load steps are applied herein.

Fig. 14 shows the contour plots of displacements in the deformed configurations. The displacements at the points A and B shown in Fig. 15 are consistent with the reference solutions [72], which

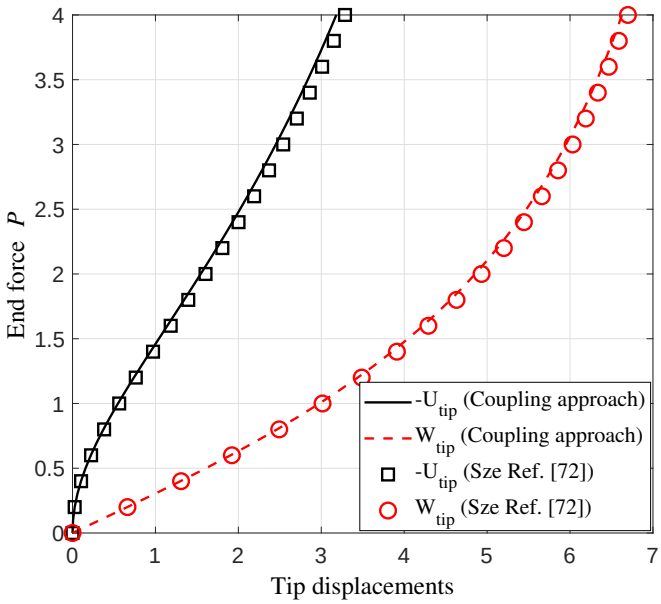


Figure 13: The load-deflection curves at the end of the cantilever plate.

verifies the exactness of the coupling approach. Furthermore, the cubic basis function converges faster than the quadratic basis function, whereas it is more time-consuming. The results presented by Duong et al. [59] show the same influence of different-order basis functions as present results.

*5.2.3. Pinched cylindrical shell*

A pinched cylindrical shell subjected to two point loadings $P = 1.2\times10^4$ N is considered. The geometry parameters are the radius $R = 200$ mm, the length $L = 200$ mm and the thickness $t = 1$ mm. The material properties are the Young's modulus $E = 3\times10^4$ N/mm$^2$ and the Poisson's ratio $\nu = 0.3$. The quadratic basis function is employed to approximate displacement fields and 40 load steps are equally applied.

The radial displacements at the points A and B shown in Fig. 16 are consistent with the reference solutions [72]. The deformed configurations at different load steps are shown in Fig. 17.

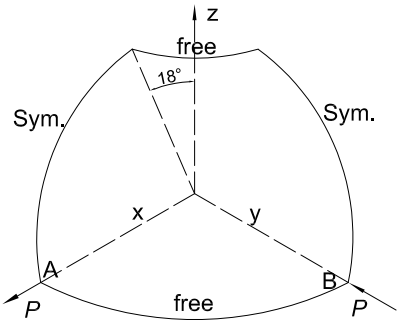


(a)

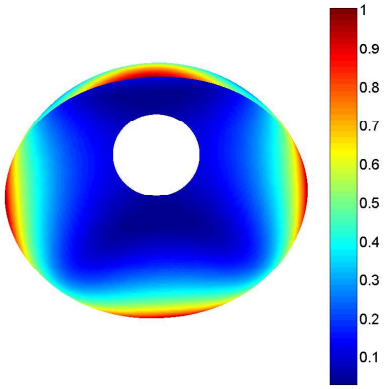


(b)

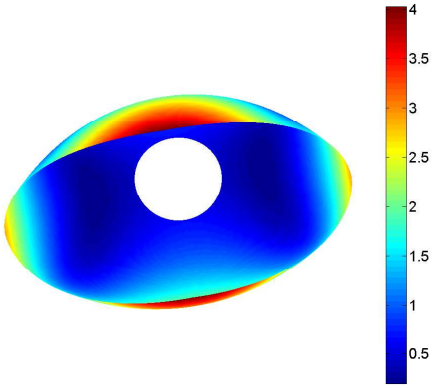


(c)

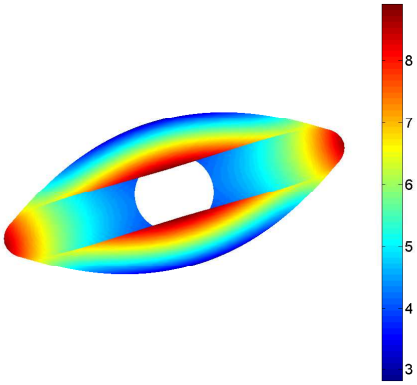


(d)

Figure 14: The hemispherical shell: (a) one quarter of the geometry; the contour plots of displacements in the deformed configurations at the load steps (b) 1, (c) 10 and (d) 40.

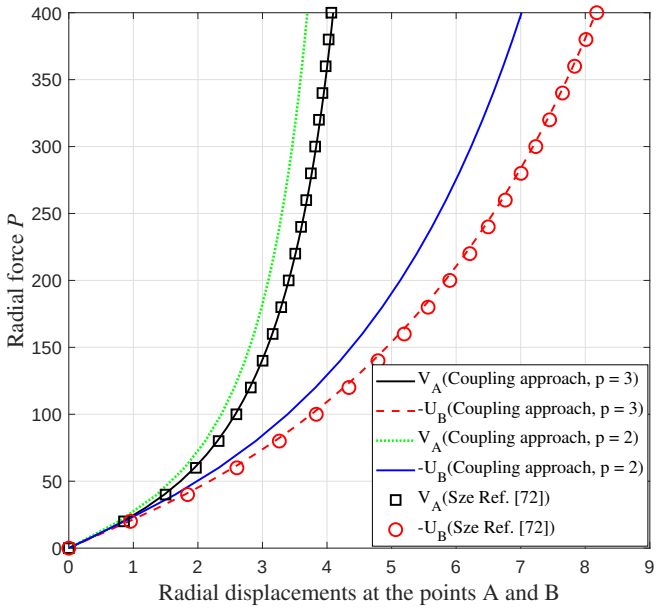


Figure 15: The load-deflection curves at the points A and B of the hemispherical shell.

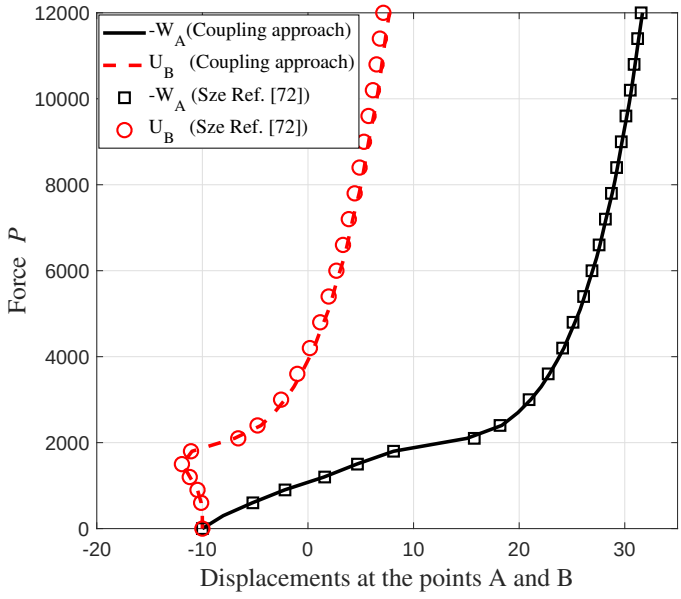


Figure 16: The load-deflection curves at the points A and B of the pinched cylindrical shell.

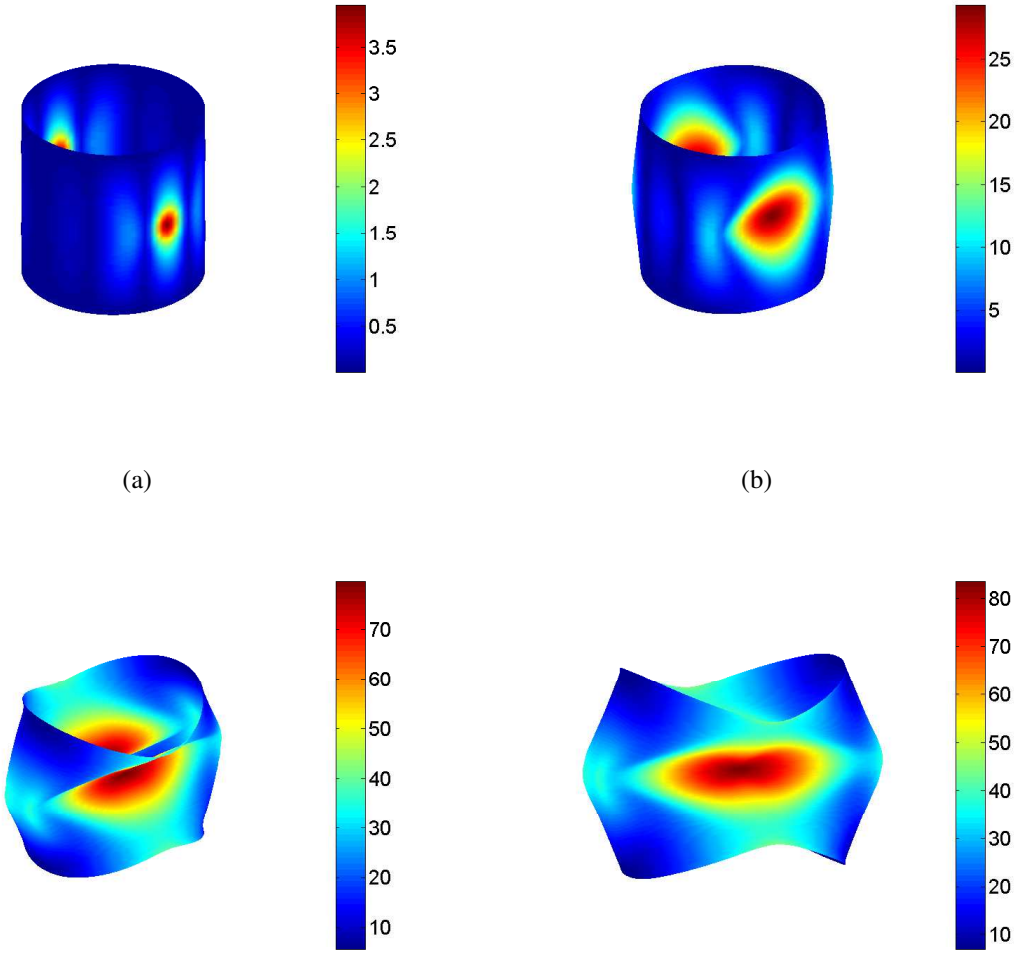


(a) (b)

(c) (d)

Figure 17: The contour plots of displacements in the deformed configurations at the load steps (a) 1, (b) 5, (c) 30 and (d) 40.

*5.2.4. Open-ended cylindrical shell*

An open-ended cylindrical shell pulled by a pair of radial forces $P = 4\times10^4$ N is shown in Fig. 18(a). The geometry parameters are the radius $R = 4.953$ mm, the length $L = 10.35$ mm and the thickness $t = 0.094$ mm. The material properties include the Young's modulus $E = 10.5\times10^6$ N/mm$^2$ and the Poisson's ratio $\nu = 0.3125$. One eighth of the shell is modeled because of the symmetry. The quadratic basis function and 20 equal load steps are applied.

The deformed cylindrical shells at the load steps 1, 5 and 20 are plotted in Fig. 18 (b)-(d), respectively. The displacements at the points A, B and C are consistent with the reference solutions [72] (Fig. 19), verifying the accuracy of the coupling approach.

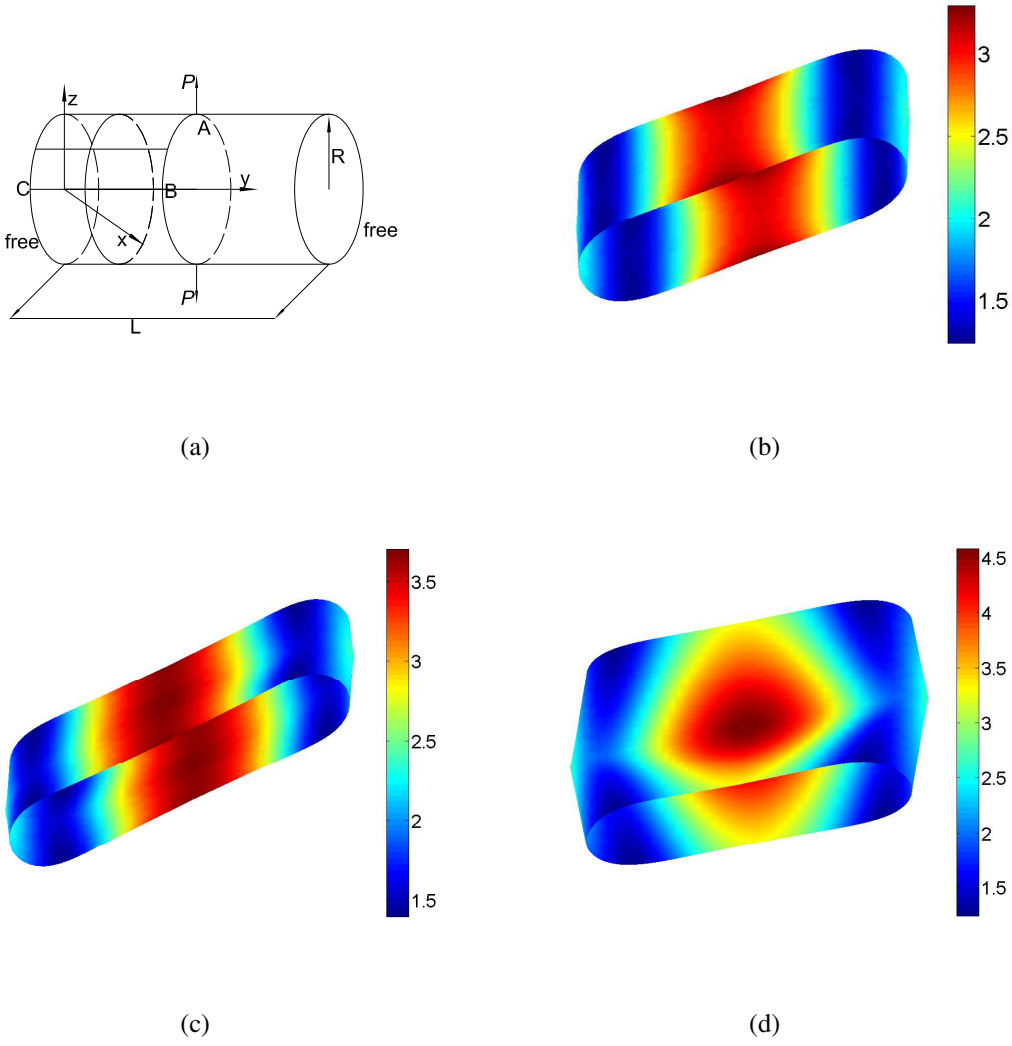


(a) (b)

(c) (d)

Figure 18: The open-ended cylindrical shell: (a) the geometry; the contour plots of displacements in the deformed configurations at the load steps (b) 1, (c) 5 and (d) 20.

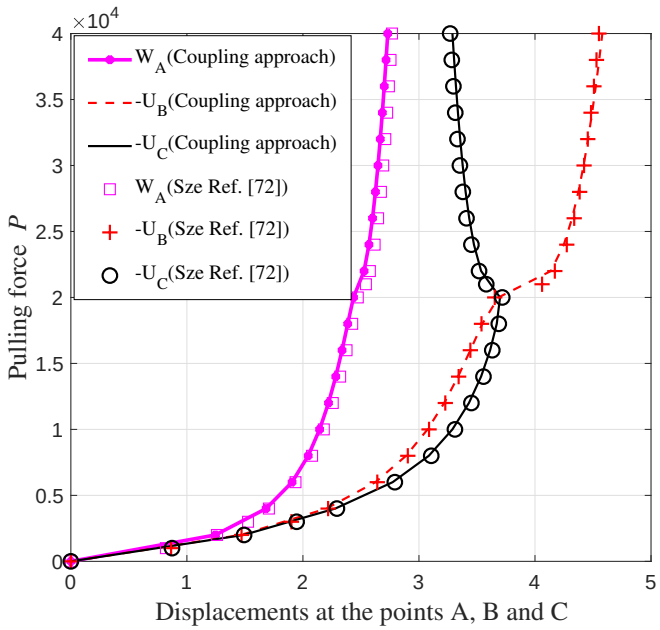


Figure 19: The load-deflection curves at the points A, B and C of the open-ended cylindrical shell.

## 6. Conclusions

In this paper, a coupling approach of the IGA and meshfree methods was developed for the geometrically linear and nonlinear elastic analyses of thin-shell structures. The coupling approach was based on the KL shell theory with the $C^1$ continuity of the displacement fields. The coupling approach utilized three subdomains: the IGA subdomain to ensure exact geometry representation, the meshfree subdomain to obtain local refinement flexibility and the coupling subdomain to guarantee smoothness between the other two subdomains. The coupling approach could converge faster than the IGA and meshfree methods by implementing local refinement. The feasibility and accuracy of the coupling approach were demonstrated by solving the benchmark problems containing both linear and nonlinear deformation.

The coupling approach with global refinement could produce more accurate results, higher convergence rate and less computational cost than the meshfree method, while achieving the same convergence rate as the IGA method. Furthermore, with the successful implementation of local refinement, the coupling approach could achieve higher convergence rates than the IGA and meshfree methods (with global refinement).

## Acknowledgments

The authors acknowledge the financial support from the Singapore Maritime Institute (Grant No: SMI-2014-MA11), and the Ministry of Education, Singapore (Academic Research Fund TIER 1-RG174/15).

## Appendix A Calculations of basis vectors and metric coefficients

In the reference configuration, the covariant basis vectors which are defined as the derivatives of point $\mathbf{X}_0$ with respect to $\xi^i\,(i=1,2,3)$ are calculated as follows:

$$\mathbf{G}_\alpha = \frac{\partial \mathbf{X}_0}{\partial \xi^\alpha} = \frac{\partial \boldsymbol{\varphi}_0}{\partial \xi^\alpha} + \xi^3 \frac{\partial \mathbf{A}_3}{\partial \xi^\alpha} = \mathbf{A}_\alpha + \xi^3 \frac{\partial \mathbf{A}_3}{\partial \xi^\alpha} \quad (\alpha = 1,2), \tag{57}$$

$$\mathbf{G}_3 = \frac{\partial \mathbf{X}_0}{\partial \xi^3} = \mathbf{A}_3. \tag{58}$$

Similarly, the covariant basis vectors in the deformed configuration are given as

$$\mathbf{g}_\alpha = \frac{\partial \mathbf{x}}{\partial \xi^\alpha} = \frac{\partial \boldsymbol{\varphi}}{\partial \xi^\alpha} + \xi^3 \frac{\partial \mathbf{a}_3}{\partial \xi^\alpha} = \mathbf{a}_\alpha + \xi^3 \frac{\partial \mathbf{a}_3}{\partial \xi^\alpha}, \tag{59}$$

$$\mathbf{g}_3 = \frac{\partial \mathbf{x}}{\partial \xi^3} = \mathbf{a}_3. \tag{60}$$

The unit normal vectors of the middle surface in the reference configuration and the deformed configuration are calculated as

$$\mathbf{A}_3 = \frac{\mathbf{A}_1 \times \mathbf{A}_2}{|\mathbf{A}_1 \times \mathbf{A}_2|} \ , \quad \mathbf{a}_3 = \frac{\mathbf{a}_1 \times \mathbf{a}_2}{|\mathbf{a}_1 \times \mathbf{a}_2|}. \tag{61}$$

The covariant metric coefficients satisfy the following equations:

$$G_{ij} = \mathbf{G}_i \cdot \mathbf{G}_j \ , \quad g_{ij} = \mathbf{g}_i \cdot \mathbf{g}_j, \tag{62}$$

$$A_{ij} = \mathbf{A}_i \cdot \mathbf{A}_j \ , \quad a_{ij} = \mathbf{a}_i \cdot \mathbf{a}_j. \tag{63}$$

The contravariant basis vectors and corresponding metric coefficients in the reference configuration and the deformed configuration are calculated as

$$\mathbf{G}^i = G^{ij}\mathbf{G}_j \ , \quad G^{ij} = \frac{1}{G_{ij}}. \tag{64}$$

$$\mathbf{A}^i = A^{ij}\mathbf{A}_j \ , \quad A^{ij} = \frac{1}{A_{ij}}, \tag{65}$$

$$\mathbf{g}^i = g^{ij}\mathbf{g}_j \ , \quad g^{ij} = \frac{1}{g_{ij}}, \tag{66}$$

$$\mathbf{a}^i = a^{ij}\mathbf{a}_j \ , \quad a^{ij} = \frac{1}{a_{ij}}. \tag{67}$$

The Green-Lagrange strain tensor is expressed as

$$\mathbf{E} = E_{ij}\mathbf{G}^i \otimes \mathbf{G}^j \ , \quad E_{ij} = \frac{1}{2}\left(g_{ij} - G_{ij}\right). \tag{68}$$

## Appendix B Linearised kinematics

The following membrane strains and bending strains can be obtained when the second derivatives of displacements are emitted:

$$\varepsilon_{\alpha\beta} = \frac{1}{2}\left(\mathbf{u}_{,\alpha}\cdot\mathbf{A}_{\beta} + \mathbf{u}_{,\beta}\cdot\mathbf{A}_{\alpha}\right), \tag{69}$$

$$\begin{aligned}\kappa_{\alpha\beta} = &-\mathbf{u}_{,\alpha\beta}\cdot\mathbf{A}_3 + \tfrac{1}{j_0}\left(\mathbf{u}_{,1}\cdot\left(\mathbf{A}_{\alpha,\beta}\times\mathbf{A}_2\right) - \mathbf{u}_{,2}\cdot\left(\mathbf{A}_{\alpha,\beta}\times\mathbf{A}_1\right)\right)\\ &+ \tfrac{\mathbf{A}_{\alpha,\beta}\cdot\mathbf{A}_3}{j_0}\left(\mathbf{u}_{,1}\cdot\left(\mathbf{A}_2\times\mathbf{A}_3\right) + \mathbf{u}_{,2}\cdot\left(\mathbf{A}_3\times\mathbf{A}_1\right)\right)\end{aligned}. \tag{70}$$

The variations of Eqs. (69) and (70) are calculated as

$$\delta\varepsilon_{\alpha\beta} = \frac{1}{2}\left(\delta\mathbf{u}_{,\alpha}\cdot\mathbf{A}_{\beta} + \delta\mathbf{u}_{,\beta}\cdot\mathbf{A}_{\alpha}\right), \tag{71}$$

$$\begin{aligned}\delta\kappa_{\alpha\beta} = &-\delta\mathbf{u}_{,\alpha\beta}\cdot\mathbf{A}_3 + \tfrac{1}{j_0}\left(\delta\mathbf{u}_{,1}\cdot\left(\mathbf{A}_{\alpha,\beta}\times\mathbf{A}_2\right) - \delta\mathbf{u}_{,2}\cdot\left(\mathbf{A}_{\alpha,\beta}\times\mathbf{A}_1\right)\right)\\ &+ \tfrac{\mathbf{A}_{\alpha,\beta}\cdot\mathbf{A}_3}{j_0}\left(\delta\mathbf{u}_{,1}\cdot\left(\mathbf{A}_2\times\mathbf{A}_3\right) + \delta\mathbf{u}_{,2}\cdot\left(\mathbf{A}_3\times\mathbf{A}_1\right)\right)\end{aligned}. \tag{72}$$

The strains can be obtained by substituting the displacement variables in Eq. (26) and the basis vectors in Eqs. (57) and (58) into Eqs. (69) and (70).

## Appendix C Derivatives of strain variables

The first derivative of a point in the middle surface with respect to the nodal displacement yields

$$\frac{\partial\boldsymbol{\varphi}}{\partial u_r} = \sum_{I=1}^{N_S}\Phi_I(\xi)\left(p_I + u_I\right)_{,r} = \sum_{I=1}^{N_S}\Phi_I(\xi)\,u_{I,r}, \tag{73}$$

and the first derivative of the covariant basis vectors is calculated as

$$\mathbf{a}_{\alpha,r} = \frac{\partial\mathbf{a}_{\alpha}}{\partial u_r} = \sum_{I=1}^{N_S}\Phi_{I,\alpha}(\xi)\,u_{I,r}. \tag{74}$$

The first derivative of the membrane strains with respect to the nodal displacement $u_r$ is

$$\frac{\partial\varepsilon_{\alpha\beta}}{\partial u_r} = \frac{1}{2}\left(\mathbf{a}_{\alpha}\cdot\mathbf{a}_{\beta} - \mathbf{A}_{\alpha}\cdot\mathbf{A}_{\beta}\right)_{,r} = \frac{1}{2}\left(\mathbf{a}_{\alpha,r}\cdot\mathbf{a}_{\beta} + \mathbf{a}_{\alpha}\cdot\mathbf{a}_{\beta,r}\right). \tag{75}$$

The second derivative of the membrane strains is

$$\frac{\partial^2\varepsilon_{\alpha\beta}}{\partial u_r\partial u_s} = \frac{1}{2}\left(\mathbf{a}_{\alpha,r}\cdot\mathbf{a}_{\beta,s} + \mathbf{a}_{\alpha,s}\cdot\mathbf{a}_{\beta,r}\right). \tag{76}$$

Several terms are calculated for the derivatives of the bending strains. The first derivative of the normal vector $\mathbf{a}_3$ defined in Eq. (61) with respect to the nodal displacement $u_r$ is calculated as

$$\mathbf{a}_{3,r} = \frac{\vec{\mathbf{a}}_{3,r}\bar{a}_3 - \vec{\mathbf{a}}_3\bar{a}_{3,r}}{\bar{a}_3^2}\quad,\quad \bar{a}_3 = |a_1\times a_2|\quad,\quad \vec{\mathbf{a}}_3 = \mathbf{a}_1\times\mathbf{a}_2, \tag{77}$$

where $\bar{a}_3$ represents the length of $\vec{\mathbf{a}}_3$, and the derivatives of $\bar{a}_{3,r}$ and $\vec{\mathbf{a}}_{3,r}$ are calculated as

$$\bar{a}_{3,r} = \frac{\vec{\mathbf{a}}_3 \vec{\mathbf{a}}_{3,r}}{\bar{a}_3} \quad , \quad \vec{\mathbf{a}}_{3,r} = \mathbf{a}_{1,r} \times \mathbf{a}_2 \ + \mathbf{a}_1 \times \mathbf{a}_{2,r}. \tag{78}$$

The derivative of $\mathbf{a}_{\alpha,\beta}$ with respect to the nodal displacement $u_r$ is given as

$$\mathbf{a}_{\alpha,\beta,r} = \sum_{I=1}^{N_S} \Phi_{I,\alpha\beta}(\xi)\, u_{I,r}. \tag{79}$$

The first derivative and second derivative of the bending strains $\kappa_{\alpha\beta}$ with respect to the nodal displacement $u_r$ can be obtained as

$$\kappa_{\alpha\beta,r} = \left(\mathbf{A}_{\alpha,\beta} \cdot \mathbf{A}_3 - \mathbf{a}_{\alpha,\beta} \cdot \mathbf{a}_3\right)_{,r} = -\mathbf{a}_{\alpha,\beta,r} \cdot \mathbf{a}_3 - \mathbf{a}_{\alpha,\beta} \cdot \mathbf{a}_{3,r}, \tag{80}$$

$$\kappa_{\alpha\beta,rs} = \left(\mathbf{A}_{\alpha,\beta} \cdot \mathbf{A}_3 - \mathbf{a}_{\alpha,\beta} \cdot \mathbf{a}_3\right)_{,rs} = -\left(\mathbf{a}_{\alpha,\beta,r} \cdot \mathbf{a}_{3,s} + \mathbf{a}_{\alpha,\beta,s} \cdot \mathbf{a}_{3,r} + \mathbf{a}_{\alpha,\beta} \cdot \mathbf{a}_{3,rs}\right). \tag{81}$$

## References


[1] S. Timoshenko and S. Woinowsky-Krieger. *Theory of Plates and Shells*. McGraw-Hill, 1959.

[2] P.M.A. Areias, J.H. Song, and T. Belytschko. A finite-strain quadrilateral shell element based on discrete Kirchhoff-Love constraints. *International Journal for Numerical Methods in Engineering*, 64(9):1166–1206, 2005.

[3] P.M.A. Areias, J.H. Song, and T. Belytschko. Analysis of fracture in thin shells by overlapping paired elements. *Computer Methods in Applied Mechanics and Engineering*, 195(41):5343–5360, 2006.

[4] D. Millan, A. Rosolen, and M. Arroyo. Thin shell analysis from scattered points with maximum-entropy approximants. *International Journal for Numerical Methods in Engineering*, 85(6):723–751, 2011.

[5] L. Noëls and R. Radovitzky. A new discontinuous Galerkin method for Kirchhoff-Love shells. *Computer Methods in Applied Mechanics and Engineering*, 197(33):2901–2929, 2008.

[6] D. Wang and J.S. Chen. Locking-free stabilized conforming nodal integration for meshfree Mindlin-Reissner plate formulation. *Computer Methods in Applied Mechanics and Engineering*, 193(12):1065–1083, 2004.

[7] D.J. Benson, Y. Bazilevs, M.C. Hsu, and T.J.R. Hughes. Isogeometric shell analysis: the Mindlin-Reissner shell. *Computer Methods in Applied Mechanics and Engineering*, 199(5):276–289, 2010.

[8] N. Nguyen-Thanh, T. Rabczuk, H. Nguyen-Xuan, and S. Bordas. A smoothed finite element method for shell analysis. *Computer Methods in Applied Mechanics and Engineering*, 198(2):165–177, 2008.

[9] T. Chau-Dinh, G. Zi, P.S. Lee, T. Rabczuk, and J.H. Song. Phantom-node method for shell models with arbitrary cracks. *Computers and Structures*, 92:242–256, 2012.

[10] J. Lasry, J. Pommier, Y. Renard, and M. Salaün. Extended finite element methods for thin cracked plates with Kirchhoff-Love theory. *International Journal for Numerical Methods in Engineering*, 84(9):1115–1138, 2010.

[11] J.C. Simo, D.D. Fox, and M.S. Rifai. On a stress resultant geometrically exact shell model. Part II: The linear theory; computational aspects. *Computer Methods in Applied Mechanics and Engineering*, 73(1):53–92, 1989.

[12] Y. Basar and Y. Ding. Finite-element analysis of hyperelastic thin shells with large strains. *Computational Mechanics*, 18(3):200–214, 1996.

[13] T.J.R. Hughes and W.K. Liu. Nonlinear finite element analysis of shells: Part I. Three-dimensional shells. *Computer Methods in Applied Mechanics and Engineering*, 26(3):331–362, 1981.

[14] T. Belytschko, H. Stolarski, W.K. Liu, N. Carpenter, and J. Ong. Stress projection for membrane and shear locking in shell finite elements. *Computer Methods in Applied Mechanics and Engineering*, 51(1-3):221–258, 1985.

[15] F. Cirak, M. Ortiz, and P. Schroder. Subdivision surfaces: a new paradigm for thin-shell finite-element analysis. *International Journal for Numerical Methods in Engineering*, 47(12):2039–2072, 2000.

[16] T. Belytschko, Y.Y. Lu, and L. Gu. Element-free Galerkin methods. *International Journal for Numerical Methods in Engineering*, 37(2):229–256, 1994.

[17] J. Kiendl, K.U. Bletzinger, J. Linhard, and R. Wüchner. Isogeometric shell analysis with Kirchhoff-Love elements. *Computer Methods in Applied Mechanics and Engineering*, 198(49):3902–3914, 2009.

[18] J.J. Monaghan. Smoothed particle hydrodynamics. *Annual review of astronomy and astrophysics*, 30(1):543–574, 1992.

[19] P. Krysl and T. Belytschko. Analysis of thin shells by the element-free Galerkin method. *International Journal of Solids and Structures*, 33(20-22):3057–3080, 1996.

[20] W.K. Liu, S. Jun, and Y.F. Zhang. Reproducing kernel particle methods. *International Journal for Numerical Methods in Fluids*, 20(8-9):1081–1106, 1995.

[21] W.K. Liu, S. Jun, S. Li, J. Adee, and T. Belytschko. Reproducing kernel particle methods for structural dynamics. *International Journal for Numerical Methods in Engineering*, 38(10):1655–1679, 1995.

[22] T. Belytschko, Y. Krongauz, D. Organ, M. Fleming, and P. Krysl. Meshless methods: an overview and recent developments. *Computer Methods in Applied Mechanics and Engineering*, 139(1-4):3–47, 1996.

[23] V.P. Nguyen, T. Rabczuk, S. Bordas, and M. Duflot. Meshless methods: a review and computer implementation aspects. *Mathematics and Computers in Simulation*, 79(3):763–813, 2008.

[24] G.R. Liu. *Meshfree methods: moving beyond the finite element method*. Taylor & Francis, 2009.

[25] G.R. Liu and Y.T. Gu. *An introduction to meshfree methods and their programming*. Springer Science & Business Media, 2005.

[26] D. Levin. The approximation power of moving least-squares. *Mathematics of Computation of the American Mathematical Society*, 67(224):1517–1531, 1998.

[27] L. Liu, G.R. Liu, and V.B.C. Tan. Element free method for static and free vibration analysis of spatial thin shell structures. *Computer Methods in Applied Mechanics and Engineering*, 191(51):5923–5942, 2002.

[28] K.M. Liew, T.Y. Ng, X. Zhao, and J.N. Reddy. Harmonic reproducing kernel particle method for free vibration analysis of rotating cylindrical shells. *Computer Methods in Applied Mechanics and Engineering*, 191(37):4141–4157, 2002.

[29] A.J.M. Ferreira, C.M.C. Roque, and R.M.N. Jorge. Static and free vibration analysis of composite shells by radial basis functions. *Engineering Analysis with Boundary Elements*, 30(9):719–733, 2006.

[30] T. Belytschko, L. Gu, and Y.Y. Lu. Fracture and crack growth by element free Galerkin methods. *Modelling and Simulation in Materials Science and Engineering*, 2(3A):519, 1994.

[31] T. Belytschko and M. Tabbara. Dynamic fracture using element-free Galerkin methods. *International Journal for Numerical Methods in Engineering*, 39(6):923–938, 1996.

[32] T. Rabczuk, P.M.A. Areias, and T. Belytschko. A meshfree thin shell method for non-linear dynamic fracture. *International Journal for Numerical Methods in Engineering*, 72(5):524–548, 2007.

[33] T. Rabczuk and P.M.A. Areias. A meshfree thin shell for arbitrary evolving cracks based on an extrinsic basis. *Computer Modeling in Engineering and Sciences*, 16(2):115–130, 2006.

[34] K.M. Liew, T.Y. Ng, and Y.C. Wu. Meshfree method for large deformation analysis-a reproducing kernel particle approach. *Engineering Structures*, 24(5):543–551, 2002.

[35] S. Li, W. Hao, and W.K. Liu. Numerical simulations of large deformation of thin shell structures using meshfree methods. *Computational Mechanics*, 25(2):102–116, 2000.

[36] Y.T. Gu, Q.X. Wang, and K.Y. Lam. A meshless local Kriging method for large deformation analyses. *Computer Methods in Applied Mechanics and Engineering*, 196(9):1673–1684, 2007.

[37] T.J.R. Hughes, J.A. Cottrell, and Y. Bazilevs. Isogeometric analysis: CAD, finite elements, NURBS, exact geometry and mesh refinement. *Computer Methods in Applied Mechanics and Engineering*, 194(39):4135–4195, 2005.

[38] M.A. Scott J.A. Evans M.J. Borden E. Rank D. Schillinger, L. Dede and T.J.R. Hughes. An isogeometric design-through-analysis methodology based on adaptive hierarchical refinement of NURBS, immersed boundary methods, and T-spline CAD surfaces. *Computer Methods in Applied Mechanics and Engineering*, 249:116–150, 2012.

[39] T.K. Uhm and S.K. Youn. T-spline finite element method for the analysis of shell structures. *International Journal for Numerical Methods in Engineering*, 80(4):507–536, 2009.

[40] R. Schmidt, R. Wüchner, and K.U. Bletzinger. Isogeometric analysis of trimmed NURBS geometries. *Computer Methods in Applied Mechanics and Engineering*, 241:93–111, 2012.

[41] J.A. Cottrell, A. Reali, Y. Bazilevs, and T.J.R. Hughes. Isogeometric analysis of structural vibrations. *Computer Methods in Applied Mechanics and Engineering*, 195:5257–5297, 2006.

[42] S. Lipton, J.A Evans, Y. Bazilevs, T. Elguedj, and T.J.R. Hughes. Robustness of isogeometric structural discretizations und severe mesh distortion. *Computer Methods in Applied Mechanics and Engineering*, 199:357–373, 2010.

[43] T.J.R. Hughes, A. Reali, and G. Sangalli. Efficient quadrature for NURBS-based isogeometric analysis. *Computer Methods in Applied Mechanics and Engineering*, 199:301–313, 2010.

[44] T.W. Sederberg, J. Zheng, A. Bakenov, and A. Nasri. T-splines and T-NURCCs. *ACM transactions on graphics (TOG)*, 22(3):477–484, 2003.

[45] T.W. Sederberg, D.L. Cardon, G.T. Finnigan, N.S. North, J. Zheng, and T. Lyche. T-spline simplification and local refinement. *ACM Transactions on Graphics (TOG)*, 23(3):276–283, 2004.

[46] Y. Bazilevs, V.M. Calo, J.A. Cottrell, J.A. Evans, T.J.R. Hughes, S. Lipton, M.A. Scott, and T.W. Sederberg. Isogeometric analysis using T-splines. *Computer Methods in Applied Mechanics and Engineering*, 199(5):229–263, 2010.

[47] M.R. Dörfel, B. Jüttler, and B. Simeon. Adaptive isogeometric analysis by local h-refinement with T-splines. *Computer Methods in Applied Mechanics and Engineering*, 199(5):264–275, 2010.

[48] H.J. Kim, Y.D. Seo, and S.K. Youn. Isogeometric analysis for trimmed CAD surfaces. *Computer Methods in Applied Mechanics and Engineering*, 198(37):2982–2995, 2009.

[49] D. Wang and H. Zhang. Reproducing kernel formulation of B-spline and NURBS basis functions: A meshfree local refinement strategy for isogeometric analysis. *Computer Methods in Applied Mechanics and Engineering*, 320:474–508, 2017.

[50] J. Kiendl, M. Ambati, L. De Lorenzis, H. Gomez, and A. Reali. Phase-field description of brittle fracture in plates and shells. *Computer Methods in Applied Mechanics and Engineering*, 312:374–394, 2016.

[51] L. Chen, N. Nguyen-Thanh, H. Nguyen-Xuan, T. Rabczuk, S. Bordas, and G. Limbert. Explicit finite deformation analysis of isogeometric membranes. *Computer Methods in Applied Mechanics and Engineering*, 277:104–130, 2014.

[52] N. Nguyen-Thanh, N. Valizadeh, M.N. Nguyen, H. Nguyen-Xuan, X. Zhuang, P. Areias, G. Zi, Y. Bazilevs, L. De Lorenzis, and T. Rabczuk. An extended isogeometric thin shell analysis based on Kirchhoff-Love theory. *Computer Methods in Applied Mechanics and Engineering*, 284:265–291, 2015.

[53] S.S. Ghorashi, N. Valizadeh, and S. Mohammadi. Extended isogeometric analysis for simulation of stationary and propagating cracks. *International Journal for Numerical Methods in Engineering*, 89(9):1069–1101, 2012.

[54] J. Kiendl, Y. Bazilevs, M.C. Hsu, R. Wüchner, and K.U. Bletzinger. The bending strip method for isogeometric analysis of Kirchhoff-Love shell structures comprised of multiple patches. *Computer Methods in Applied Mechanics and Engineering*, 199(37):2403–2416, 2010.

[55] Y. Guo and M. Ruess. Nitsche's method for a coupling of isogeometric thin shells and blended shell structures. *Computer Methods in Applied Mechanics and Engineering*, 284:881–905, 2015.

[56] D.J. Benson, Y. Bazilevs, M.C. Hsu, and T.J.R. Hughes. A large deformation, rotation-free, isogeometric shell. *Computer Methods in Applied Mechanics and Engineering*, 200(13):1367–1378, 2011.

[57] N. Nguyen-Thanh, J. Kiendl, H. Nguyen-Xuan, R. Wüchner, K.U. Bletzinger, Y. Bazilevs, and T. Rabczuk. Rotation free isogeometric thin shell analysis using PHT-splines. *Computer Methods in Applied Mechanics and Engineering*, 200(47):3410–3424, 2011.

[58] N. Nguyen-Thanh, K. Zhou, X. Zhuang, P. Areias, H. Nguyen-Xuan, Y. Bazilevs, and T. Rabczuk. Isogeometric analysis of large-deformation thin shells using RHT-splines for multiple-patch coupling. *Computer Methods in Applied Mechanics and Engineering*, 316:1157–1178, 2017.

[59] T.X. Duong, F. Roohbakhshan, and R.A. Sauer. A new rotation-free isogeometric thin shell formulation and a corresponding continuity constraint for patch boundaries. *Computer Methods in Applied Mechanics and Engineering*, 316:43–83, 2017.

[60] B.N. Rao and S. Rahman. A coupled meshless-finite element method for fracture analysis of cracks. *International Journal of Pressure Vessels and Piping*, 78(9):647–657, 2001.

[61] T. Rabczuk, S. Xiao, and M. Sauer. Coupling of mesh-free methods with finite elements: basic concepts and test results. *International Journal for Numerical Methods in Biomedical Engineering*, 22(10):1031–1065, 2006.

[62] T. Belytschko, D. Organ, and Y. Krongauz. A coupled finite element-element-free Galerkin method. *Computational Mechanics*, 17(3):186–195, 1995.

[63] D. Wang and H. Zhang. A consistently coupled isogeometric-meshfree method. *Computer Methods in Applied Mechanics and Engineering*, 268:843–870, 2014.

[64] N. Valizadeh, Y. Bazilevs, J.S. Chen, and T. Rabczuk. A coupled IGA-Meshfree discretization of arbitrary order of accuracy and without global geometry parameterization. *Computer Methods in Applied Mechanics and Engineering*, 293:20–37, 2015.

[65] A. Rosolen and M. Arroyo. Blending isogeometric analysis and local maximum entropy meshfree approximants. *Computer Methods in Applied Mechanics and Engineering*, 264:95–107, 2013.

[66] L. Piegl and W. Tiller. *The NURBS book*. Springer Science & Business Media, 2012.

[67] D.F. Rogers. *An introduction to NURBS: with historical perspective*. Elsevier, 2000.

[68] J.C. Simo and D.D. Fox. On a stress resultant geometrically exact shell model. Part I: Formulation and optimal parametrization. *Computer Methods in Applied Mechanics and Engineering*, 72(3):267–304, 1989.

[69] T. Belytschko, W.K. Liu, B. Moran, and K. Elkhodary. *Nonlinear finite elements for continua and structures*. John Wiley & Sons, 2013.

[70] A. Ben-Israel. A Newton-Raphson method for the solution of systems of equations. *Journal of Mathematical Analysis and Applications*, 15(2):243–252, 1966.

[71] T Rabczuk and Ted Belytschko. Adaptivity for structured meshfree particle methods in 2d and 3d. *International Journal for Numerical Methods in Engineering*, 63(11):1559–1582, 2005.

[72] K.Y. Sze, X.H. Liu, and S.H. Lo. Popular benchmark problems for geometric nonlinear analysis of shells. *Finite Elements in Analysis and Design*, 40(11):1551–1569, 2004.